Combustion and Flame 207 (2019) 153–170

Contents lists available at ScienceDirect

Combustion and Flame

journal homepage: www.elsevier.com/locate/combustflame

Chemo-thermal model and Gaussian process emulator for combustion synthesis of Ni/Al composites

Mohammad Shabouei[a], Waad Subber[a], Cedric W. Williams[a,b], Karel Matouš[a,b,*], Joseph M. Powers[a,b]

[a] Center for Shock Wave-processing of Advanced Reactive Materials (C-SWARM), United States
[b] Department of Aerospace and Mechanical Engineering, University of Notre Dame, Notre Dame, IN 46556, United States

ARTICLE INFO

Article history:
Received 10 January 2019
Revised 8 March 2019
Accepted 22 May 2019

Keywords:
Chemo-thermal model
Ni and Al combustion
Combustion synthesis
Bayesian calibration
Thermodynamics
Gaussian process emulator

ABSTRACT

We propose a chemo-thermal model that considers both diffusion and reaction phenomena, consumption and formation of species, and heat generation due to chemical reactions. We study the thermal and chemical processes in combustion of heterogeneous reactive materials at the microstructural level. The model is applied to the combustion of Nickel and Aluminum (Ni/Al) composites. We provide numerical results such as the reaction front speed, reaction time, and temperature evolution during reaction and compare those with the existing experimental data. Sensitivity analysis and Bayesian calibration of the diffusion and reaction parameters are performed. We show that both diffusion and reaction are strongly coupled in thin zones such that neither can be neglected. Moreover, a multi-fidelity and multi-scale Gaussian process emulator is developed to overcome the computational cost of the simulations at different length-scales.

1. Introduction

Combustion of condensed phase reactive systems has been studied for fabricating and processing a wide variety of advanced materials such as alloys [1,2], intermetallic compounds [3–5], complex oxides [6–8], super hard materials [9], and biological materials [10,11]. Combustion synthesis (CS) [12] also has numerous practical applications including in electronic devices [13,14], battery and energy materials [15,16], and drug delivery [17,18]. CS is often characterized by self-propagating and high temperature processes [19], sharp gradients, rapid self-sustained reaction waves, and intense heat release [20,21]. There are two distinct initiation cases for CS. In the first, a highly exothermic reaction is initiated locally by a thermal impulse which leads to the formation of a self-propagating high-temperature synthesis wave [14,22]. In the second case, an exothermic reaction is induced uniformly throughout the whole volume of the composite and a spatially homogeneous thermal explosion takes place [3,23].

Numerous works have investigated CS to elucidate the mechanisms and processes using theoretical [24,25], experimental [23,26], or numerical [21,27] approaches. Merzhanov [28] extended the theory of condensed phase combustion [29] to self-propagating high-temperature synthesis. Then, this theory has been applied to study combustion stability [30], unsteady processes such as pulsating [31] and spinning [32] combustion, and effects of competing reactions [33]. Early theoretical models also considered the flame velocity and its dependency on the layer thickness and described the exothermic effects [34–36]. However, the reaction mechanisms and combustion characteristics that influence the process, especially at the microstructural level, are still not fully understood [27,37]. A common simplified approach for the numerical study of CS is to ignore the microstructural morphology and assume spatially homogeneous material properties [24,35]. This approach is based on classical coarse-grained models that consider the overall reaction rate [27] so that the system is represented by mean-field variables. Although this approach is reasonably accurate when the length-scale is small, it cannot capture complex dynamics interacting with material morphology. Another approach provides simplification through model reduction by means of a diffusion equation for the concentrations and a one-dimensional form of the energy equation [22,25,38]. Such models ignore heat losses, temperature variations in the direction perpendicular to the chemical front, and assume a diffusion-limited mechanism neglecting detailed coupling between reaction and diffusion processes. However, experimental studies [39,40] have shown that the microstructure and material heterogeneity play an important role on the reaction mechanisms and kinetic processes. Therefore, a detailed chemo-thermal model with both diffusion

* Corresponding author at: Department of Aerospace and Mechanical Engineering, University of Notre Dame, Notre Dame, IN 46556, United States.
E-mail address: kmatous@nd.edu (K. Matouš).

https://doi.org/10.1016/j.combustflame.2019.05.038
0010-2180/

and kinetics equations that respect the material morphology is needed.

It is worth noting that the initial heterogeneous microstructures are typically fabricated using different techniques such as cold-rolling [41,42] and high-energy ball milling (HEBM) [43,44]. For example, HEBM as a mechanical activation process is used to enhance reactivity of materials by drastically increasing the interfacial area between constituents and reducing the required diffusion length-scale [26,45,46].

The objective of this work is to study combustion in heterogeneous materials induced by a thermal stimulus that respects the detailed microstructure and coupled reaction-diffusion processes at that scale. In particular, attention is given to the mechanically activated microstructures (i.e., HEBM composites) with lower activation energies and solid state combustion processes. We also focus on a simple (i.e., a single particle) microstructure with micron length-scales rather than nano-foils or nano-composites, due to the large computational cost of these fine length-scale simulations. Resolving the essential time- and length-scales of microstructures with multiple particles or nanostructures requires highly parallel computational strategies [47,48]. We provide temperature, phase formation and combustion characteristics such as the reaction front speed, reaction time, and temperature increment during chemical process. To do so, a detailed two-way coupled thermodynamically consistent chemo-thermal model for combustion of reactive solids is presented. We consider both reaction and diffusion processes in the proposed model. The diffusion model in this work is volumetric diffusion through reactants and products. The model can capture thermal and chemical processes in both homogeneous and heterogeneous systems. Moreover, because we only consider a single particle, we neglect particle-to-particle surface physics. Then, the model is implemented in a robust multi-physics finite element solver, *iSim* [49], which is part of the *PGFem3D's* computational suite [47,48,50].

For a given set of material properties, reaction and diffusion parameters, and microstructure geometry, the solver provides temporally and spatially resolved quantities including temperature, concentrations, and reaction rates. The model is applied to the formation of NiAl with Bayesian calibration and sensitivity analysis of the diffusion and reaction parameters. The sensitivity analysis illustrates that both diffusion and reaction are essential components. We also study the effect of microstructure and provide detailed numerical simulations which highlight the capabilities of the multi-physics solver. Furthermore, we use a Bayesian framework [51,52] to infer the material properties and the underlying length-scale of the microstructure from measurement data. In the Bayesian framework, prior knowledge of the material properties and the length-scale of the microstructure is updated to posterior using response from the solver. To reduce the computational cost of the Bayesian analysis, we develop a multi-fidelity and multi-scale Gaussian process emulator [52,53]. The emulator is constructed by utilizing a small number of runs on a heterogeneous domain and a large number of runs on a premixed domain.

The remainder of the manuscript is organized as follows. Section 2 is devoted to the proposed model and the governing and constitutive equations. It also provides specification of the model for the Ni–Al reactive system. Section 3 presents the finite element weak forms and the computational framework/implementation of governing equations. Sensitivity analysis and Bayesian calibration of the parameters, effect of microstructure, the multi-fidelity and multi-scale Gaussian process emulator, and the results from a detailed numerical simulation are presented in Section 4. Finally, conclusions and future directions are drawn in Section 5.

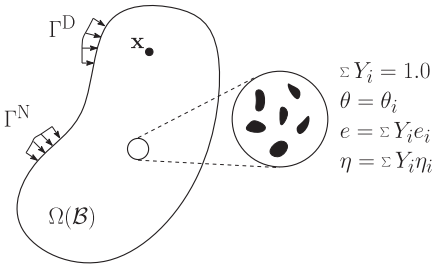

Fig. 1. An arbitrary multi-phase body $\mathcal{B}$ and computational domain Ω, partitioned by two Γ^{D} and Γ^{N} boundaries.

2. Governing equations

We first provide a concise presentation of the equations used to model our system. Our model is built in the context of a classical continuum mixture theory. More details can be found in [54–56]. We consider an open thermodynamic system in which diffusive heat and mass transfer can occur within the domain and across the boundary. Let $\mathbf{x}$ be a spatial point within a multi-phase body $\mathcal{B}$ in a configuration $\Omega(\mathcal{B}) \subset \mathbb{R}^{\mathrm{d}}$, where d denotes the number of spatial dimensions (see Fig. 1). We assume that the body does not deform. The divergence and gradient with respect to $\mathbf{x}$ are denoted by $\nabla\cdot(\bullet)$ and $\nabla(\bullet)$. The boundary of the domain, $\partial\Omega$, is partitioned by Dirichlet, Γ^{D}, and Neumann, Γ^{N}, boundaries such that $\Gamma^{\mathrm{D}} \cap \Gamma^{\mathrm{N}} = \emptyset$ and $\Gamma^{\mathrm{D}} \cup \Gamma^{\mathrm{N}} = \partial\Omega$. Here, $\mathbf{n}(\mathbf{x})$ denotes the unit outward normal to the boundary. We denote time by $t \in (0, \mathcal{T}]$ where $\mathcal{T}$ is the time interval of interest.

Now, we describe the governing equations for the coupled chemo-thermal model. Conservation of mass takes the form

$$\frac{\partial \rho}{\partial t} + \nabla \cdot (\rho \mathbf{v}(\mathbf{x}, t)) = 0 \qquad \text{in} \quad \Omega \times (0, \mathcal{T}], \tag{1}$$

where ρ is the mixture density and $\mathbf{v}$ is the mass-averaged mixture velocity. We consider cases where there is no bulk mixture motion. Because we focus on chemo-thermal behavior of reactive materials, there is also no material deformation. Therefore, $\mathbf{v} = \mathbf{0}$. As a consequence $\partial\rho/\partial t = 0$. Moreover, there is no work due to deformation, nor volume change in the material.

We make the further assumption that $\rho =$ constant for all space and time. This represents a modeling compromise for mixtures like Ni, Al, and NiAl where each material has a distinct density.

The conservation of energy (the first law of thermodynamics) is given by

$$\rho \dot{e}(\mathbf{x}, t) = -\nabla \cdot {}^{\mathrm{q}}\mathbf{j}(\mathbf{x}, t) \qquad \text{in} \quad \Omega \times (0, \mathcal{T}], \tag{2}$$

where e is the specific mixture internal energy, ${}^{\mathrm{q}}\mathbf{j}$ is the diffusive energy flux, and the superposed dot indicates the material time derivative. Because the velocity is equal to zero, the material derivative is simply $\partial/\partial t$. In Section 2.2, we will show that the energy equation can be expressed in terms of temperature θ, as

$$\rho c \dot{\theta}(\mathbf{x}, t) + \nabla \cdot {}^{\mathrm{q}}\mathbf{j}(\mathbf{x}, t) = {}^{\mathrm{c}}q(\mathbf{x}, t) \qquad \text{in} \quad \Omega \times (0, \mathcal{T}], \tag{3a}$$

$$\theta(\mathbf{x}, t) = \widetilde{\theta}(\mathbf{x}, t) \qquad \text{on} \quad \Gamma^{\mathrm{D}} \times (0, \mathcal{T}], \tag{3b}$$

$${}^{\mathrm{q}}\mathbf{j} \cdot \mathbf{n} = \widetilde{j}(\mathbf{x}, t) \qquad \text{on} \quad \Gamma^{\mathrm{N}} \times (0, \mathcal{T}], \tag{3c}$$

$$\theta(\mathbf{x}, t = 0) = \theta|_{t=0}(\mathbf{x}) \qquad \text{in} \quad \Omega, \tag{3d}$$

where $c = c_v = c_p$ is the mass-averaged specific heat of the mixture at constant volume and pressure, and ${}^{\mathrm{c}}q$ is the chemical heating term. Here, $\widetilde{\theta}$ and $\widetilde{j}$ are the prescribed temperature and heat flux

on the boundary, and $\theta|_{t=0}$ is the initial temperature. The evolution of N_s chemical species takes the form

$$\rho\dot{Y}_i(\mathbf{x},t) + \nabla\cdot {}^{\mathrm{m}}\mathbf{j}_i(\mathbf{x},t) = M_i\,\dot{\omega}_i(\mathbf{x},t) \qquad \text{in} \quad \Omega\times(0,\mathcal{T}], \tag{4a}$$

$$Y_i(\mathbf{x},t) = \widetilde{Y}_i(\mathbf{x},t) \qquad \text{on} \quad \Gamma_i^{\mathrm{D}}\times(0,\mathcal{T}], \tag{4b}$$

$${}^{\mathrm{m}}\mathbf{j}_i\cdot\mathbf{n} = 0 \qquad \text{on} \quad \Gamma_i^{\mathrm{N}}\times(0,\mathcal{T}], \tag{4c}$$

$$Y_i(\mathbf{x},t=0) = Y_i|_{t=0}(\mathbf{x}) \qquad \text{in} \quad \Omega, \tag{4d}$$

where Y_i, ${}^{\mathrm{m}}\mathbf{j}_i$, M_i, and $\dot{\omega}_i$ are mass fraction, diffusive mass flux, molecular mass, and molar rate of production/consumption of ith chemical species for $i=1,2,\ldots,N_s$, respectively. Here, $\widetilde{Y}_i$ is the ith prescribed mass fraction and $Y_i|_{t=0}$ is the initial mass fractions.

We adopt the following properties of a multi-component mixture [57,58] with N_s species

$$\theta=\theta_i,\ \sum_{i=1}^{N_s}Y_i=1,\ e=\sum_{i=1}^{N_s}Y_ie_i,\ c=\sum_{i=1}^{N_s}Y_i\,c_i,$$
$$\psi=\sum_{i=1}^{N_s}Y_i\psi_i,\ \eta=\sum_{i=1}^{N_s}Y_i\,\eta_i,\ \text{and}\ h=\sum_{i=1}^{N_s}Y_ih_i, \tag{5}$$

where ψ, η, and h, are the Helmholtz free energy, entropy, and enthalpy of the mixture, and the subscript i indicates a property of the ith species. The entropy and enthalpy of species i can be expressed as

$$\eta_i = \eta_{0,i} + c_i\ln\left[\frac{\theta}{\theta_0}\right] - \frac{R}{M_i}\ln[y_i], \tag{6a}$$

$$h_i = h_{0,i} + c_i(\theta-\theta_0), \tag{6b}$$

where $\eta_{0,i}$ and $h_{0,i}$ are the entropy and heat of formation for species i at reference temperature θ_0. Here, $y_i = (Y_i/M_i)/\sum_{j=1}^{N_s}\left(Y_j/M_j\right)$ are the species mole fractions, $\sum_{i=1}^{N_s}y_i=1$, and $R=8.314\,\mathrm{J/(mol\cdot K)}$ is the universal gas constant. In this work, $\theta|_{t=0}=\theta_0$. Finally, the mixture thermal conductivity λ is defined as

$$\lambda = \sum_{i=1}^{N_s}Y_i\lambda_i, \tag{7}$$

where λ_i is the conductivity of component i.

2.1. Constitutive equations

We shall consider energy flux as the sum of the heat conduction and the enthalpy transported by mass diffusion [54,56]

$${}^{\mathrm{q}}\mathbf{j} = \mathbf{q} + \sum_{i=1}^{N_s}h_i\,{}^{\mathrm{m}}\mathbf{j}_i. \tag{8}$$

the heat conduction, $\mathbf{q}$, is taken to be governed by the Fourier model

$$\mathbf{q} = -\lambda\nabla\theta. \tag{9}$$

similarly, we consider Fickian diffusion [59,60] for mass transfer

$${}^{\mathrm{m}}\mathbf{j}_i = -\rho D(\theta)\nabla Y_i, \tag{10}$$

where $\sum_{i=1}^{N_s}{}^{\mathrm{m}}\mathbf{j}_i = -\rho D\nabla\left(\sum_{i=1}^{N_s}Y_i\right)=0$. Here, $D(\theta)$ is a volumetric mass diffusivity with an Arrhenius-like temperature dependency [61,62] given by

$$D(\theta) = D_0\exp\left[-\frac{E_d}{R\theta}\right], \tag{11}$$

where D_0 is the diffusion pre-exponent and E_d is the diffusion activation energy.

We assume each of the N_s species evolve in N_r reactions dictated by the law of mass action whose rates have temperature-sensitivity dictated by an Arrhenius law as

$$\dot{\omega}_i = \sum_{k=1}^{N_r}\nu_{ik}\,r_k, \tag{12a}$$

$$r_k = k_k(\theta)\prod_{j=1}^{N_s}\left(\frac{\rho Y_j}{M_j}\right)^{\nu'_{jk}}\left(1-\frac{1}{K_{\mathrm{eq}_k}(\theta)}\prod_{j=1}^{N_s}\left(\frac{\rho Y_j}{M_j}\right)^{\nu_{jk}}\right), \tag{12b}$$

$$k_k = A_k\exp\left[-\frac{E_k}{R\theta}\right], \tag{12c}$$

$$K_{\mathrm{eq}_k} = \exp\left[\frac{-\Delta G_k^0}{R\theta}\right], \tag{12d}$$

where r_k is molar rate of reaction in the kth reaction. Here, ν'_{ik} is the forward stoichiometric coefficient of ith reactant in the kth reaction and ν''_{ik} is the reverse stoichiometric coefficient of the ith product in the kth reaction, and both are non-negative numbers. We also denote $\nu_{ik}=\nu''_{ik}-\nu'_{ik}$, the net stoichiometric coefficient. Here, A_k, k_k, K_{eq_k} and E_k are the collision frequency coefficient, forward and equilibrium reaction rate coefficient, and chemical kinetics activation energy of the kth reaction, respectively. Also, $\Delta G_k^0=\sum_{i=1}^{N_s}\nu_{ik}g_i$ is the net change of the Gibbs free energy, and $g_i=h_i-\theta\eta_i$ is the Gibbs free energy for species i.

2.2. Thermodynamics

Considering the Legendre transformation $e=\psi+\eta\theta$, the time rate of change of internal energy is

$$\dot{e} = \dot{\psi}+\dot{\eta}\,\theta+\eta\,\dot{\theta}. \tag{13}$$

the entropy of mixture is defined [57] as

$$\eta = -\frac{\partial\psi}{\partial\theta} \tag{14}$$

and its time derivative from Eq. (6a) and using $\eta=\sum_{i=1}^{N_s}Y_i\eta_i$ from Eq. (5), is

$$\begin{aligned}\dot{\eta} &= \sum_{i=1}^{N_s}\dot{Y}_i\eta_i + \sum_{i=1}^{N_s}Y_i\dot{\eta}_i\\ &= \sum_{i=1}^{N_s}\dot{Y}_i\eta_i + \sum_{i=1}^{N_s}Y_i\left(c_i\frac{\dot{\theta}}{\theta}-\frac{R}{M_i}\frac{\dot{y}_i}{y_i}\right)\\ &= \sum_{i=1}^{N_s}\dot{Y}_i\eta_i + c\frac{\dot{\theta}}{\theta}-\frac{R}{M}\sum_{i=1}^{N_s}\dot{y}_i.\end{aligned}$$

because $\sum_{i=1}^{N_s}y_i=1$, $\sum_{i=1}^{N_s}\dot{y}_i=0$. Thus

$$\dot{\eta} = \sum_{i=1}^{N_s}\dot{Y}_i\eta_i + c\frac{\dot{\theta}}{\theta}. \tag{15}$$

Defining $\psi=\psi(\theta,Y_i)$, the time derivative of the mixture Helmholtz free energy by using Eq. (14) is

$$\begin{aligned}\dot{\psi} &= \frac{\partial\psi}{\partial\theta}\dot{\theta}+\sum_{i=1}^{N_s}\frac{\partial\psi}{\partial Y_i}\dot{Y}_i,\\ &= -\eta\dot{\theta}+\sum_{i=1}^{N_s}\frac{\partial\psi}{\partial Y_i}\dot{Y}_i.\end{aligned} \tag{16}$$

now, substituting Eqs. (13)–(16), into Eq. (2), the balance of energy reads

$$\rho c\dot{\theta}+\nabla\cdot{}^{\mathrm{q}}\mathbf{j} = {}^{\mathrm{c}}q, \tag{17}$$

where the chemical heat ${}^{\mathrm{c}}q$ is defined as

$${}^{\mathrm{c}}q = -\rho\sum_{i=1}^{N_s}\left(\eta_i\theta+\frac{\partial\psi}{\partial Y_i}\right)\dot{Y}_i. \tag{18}$$

We may define $\frac{\partial \psi}{\partial Y_i} = \mu_i - \mu_{N_s}$ [63]. Here, μ_i and μ_{N_s} are the chemical potentials of the ith and N_sth species, respectively. So, the chemical heat ${}^{c}q$ becomes

$$
\begin{aligned}
{}^{c}q &= -\rho \sum_{i=1}^{N_s} (\eta_i \theta + \mu_i - \mu_{N_s}) \dot{Y}_i, \\
&= -\rho \sum_{i=1}^{N_s} (\eta_i \theta + \mu_i) \dot{Y}_i - \rho N_s \mu_{N_s} \sum_{i=1}^{N_s} \dot{Y}_i.
\end{aligned}
$$

recalling $\sum_{i=1}^{N_s} Y_i = 1$, one gets $\sum_{i=1}^{N_s} \dot{Y}_i = 0$. Thus, the chemical heat reads

$$
{}^{c}q = -\rho \sum_{i=1}^{N_s} (\eta_i \theta + \mu_i) \dot{Y}_i. \tag{19}
$$

upon substituting the balance of species (Eq. (4a)) into Eq. (19) and using the fact that $h_i = \eta_i \theta + \mu_i$, we get

$$
{}^{c}q = -\sum_{i=1}^{N_s} h_i (M_i \dot{\omega}_i - \nabla \cdot {}^{m}\mathbf{j}_i). \tag{20}
$$

Now, we can expand the balance of energy, Eq. (17), by substituting ${}^{q}\mathbf{j}$ from Eqs. (8)–(10) and ${}^{c}q$ from (20), and rearrange it to get

$$
\rho c \dot{\theta} - \nabla \cdot (\lambda \nabla \theta) + \sum_{i=1}^{N_s} \nabla \cdot (h_i {}^{m}\mathbf{j}_i) = -\sum_{i=1}^{N_s} (h_i M_i \dot{\omega}_i - h_i \nabla \cdot {}^{m}\mathbf{j}_i) \tag{21a}
$$

$$
\rho c \dot{\theta} - \nabla \cdot (\lambda \nabla \theta) + \sum_{i=1}^{N_s} {}^{m}\mathbf{j}_i \cdot \nabla h_i = -\sum_{i=1}^{N_s} h_i M_i \dot{\omega}_i \tag{21b}
$$

$$
\rho c \dot{\theta} - \nabla \cdot (\lambda \nabla \theta) + \sum_{i=1}^{N_s} c_i {}^{m}\mathbf{j}_i \cdot \nabla \theta = -\sum_{i=1}^{N_s} h_i M_i \dot{\omega}_i \tag{21c}
$$

$$
\rho c \dot{\theta} - \nabla \cdot (\lambda \nabla \theta) - \rho D \sum_{i=1}^{N_s} c_i \nabla Y_i \cdot \nabla \theta = -\sum_{i=1}^{N_s} h_i M_i \dot{\omega}_i \tag{21d}
$$

$$
\rho c \dot{\theta} - \nabla \cdot (\lambda \nabla \theta) - \rho D \nabla c \cdot \nabla \theta = -\sum_{i=1}^{N_s} h_i M_i \sum_{k=1}^{N_r} \nu_{ik} r_k. \tag{21e}
$$

appendix A shows that the proposed chemo-thermal model obeys the second law of thermodynamics.

2.3. Specification for Ni–Al combustion

A detailed Ni and Al reaction mechanism, based on the phase diagram [3], occurs through intermediate phases such as $NiAl_3$, Ni_2Al_3, and Ni_3Al. Also, NiAl can form directly if the reaction is initiated at temperature higher than the Al melting point [64,65]. In this work, we consider the solid state reaction process and neglect the intermediate phases to simplify the model calibration and subsequent simulations. Thus, we consider one step reaction for Ni and Al as

$$
\mathrm{Ni} + \mathrm{Al} \longrightarrow \mathrm{NiAl}. \tag{22}
$$

Although quite simple, we will show that this single step reaction mechanism provides reasonable understanding of NiAl formation. The energy equation, Eq. (21e), takes the form

$$
\rho c \frac{\partial \theta}{\partial t} - \nabla \cdot (\lambda \nabla \theta) - \rho D \nabla c \cdot \nabla \theta = -\Delta H_k r_k, \tag{23}
$$

Table 1
Properties of Ni, Al, and NiAl.

Parameter	Ni	Al	NiAl
M_i [$\frac{kg}{mol}$]	0.0587	0.027	0.0857
c_i [$\frac{kJ}{kg\,K}$]	0.444 [66]	0.89 [66]	0.537 [67]
λ_i [$\frac{kW}{m\,K}$]	0.091 [68]	0.237 [69]	0.09 [70]
$M_i h_{0,i}$ [$\frac{kJ}{mol}$]	0 [71]	0 [71]	−72 [72]

where the rate of reaction r_k is

$$
r_k = A_k \exp\left[-\frac{E_k}{R\theta}\right] \frac{\rho Y_{\mathrm{Ni}}}{M_{\mathrm{Ni}}} \frac{\rho Y_{\mathrm{Al}}}{M_{\mathrm{Al}}}. \tag{24}
$$

here, $\Delta H_k = \sum_{i=1}^{N_s} M_i h_i \nu_{ik}$ is the heat of reaction [54,56].
the chemical species equation, Eq. (4a), for Ni and Al reads

$$
\rho \frac{\partial Y_{\mathrm{Ni}}}{\partial t} - \nabla \cdot (\rho D \nabla Y_{\mathrm{Ni}}) = -M_{\mathrm{Ni}} r_k, \tag{25a}
$$

$$
\rho \frac{\partial Y_{\mathrm{Al}}}{\partial t} - \nabla \cdot (\rho D \nabla Y_{\mathrm{Al}}) = -M_{\mathrm{Al}} r_k. \tag{25b}
$$

finally, the conservation of mass, Eq. (1), reduces to

$$
\sum_{i=1}^{3} Y_i = 1, \tag{26}
$$

by which we obtain the mass fraction of NiAl (i.e., Y_{NiAl}).

Using Ni and Al properties provided in Table 1, for a stoichiometric Ni–Al reactive microstructure, 39.723% of the volume is occupied by Ni and 60.277% by Al. For $\rho_{\mathrm{Ni}} = 8.908 \times 10^3\ \mathrm{kg/m^3}$ and $\rho_{\mathrm{Al}} = 2.700 \times 10^3\ \mathrm{kg/m^3}$, the value of the constant mixture density, ρ, is

$$
\rho = 0.397 \rho_{\mathrm{Ni}} + 0.603 \rho_{\mathrm{Al}} = 5.165 \times 10^3\ \frac{\mathrm{kg}}{\mathrm{m^3}}. \tag{27}
$$

all other mixture properties including c and λ follow mixture rules in Eq. (5) and are nonuniform in space and time.

3. Numerical implementation

To employ the finite element method and solve Eqs. (23) and (25), we introduce the following function spaces for the temperature field

$$
\mathcal{S}^t := \left\{ \theta(\mathbf{x}, t) \in H^1(\Omega) \;\middle|\; \theta(\mathbf{x}, t) = \widetilde{\theta}(\mathbf{x}, t) \text{ on } \Gamma^{\theta} \times (0, \mathcal{T}] \right\}, \tag{28a}
$$

$$
\mathcal{U} := \left\{ u(\mathbf{x}) \in H^1(\Omega) \;\middle|\; u(\mathbf{x}) = 0 \text{ on } \Gamma^{\theta} \right\}, \tag{28b}
$$

and concentration fields

$$
\mathcal{Y}_i^t := \left\{ Y_i(\mathbf{x}, t) \in H^1(\Omega) \;\middle|\; Y_i(\mathbf{x}, t) = \widetilde{Y}_i(\mathbf{x}, t) \text{ on } \Gamma^{Y_i} \times (0, \mathcal{T}] \right\}, \tag{29a}
$$

$$
\mathcal{V}_i := \left\{ v_i(\mathbf{x}) \in H^1(\Omega) \;\middle|\; v_i(\mathbf{x}) = 0 \text{ on } \Gamma^{Y_i} \right\}, \tag{29b}
$$

where $H^1(\Omega)$ is a standard Sobolev space [73]. Here, we assume that the initial/boundary-value problem admits a solution in the defined spaces and make no attempt to address issues of existence and uniqueness of the solution. We replace the continuous spaces by their discrete counterparts and construct a numerical approximation of the solution. The standard L_2 inner-product for given two fields $a(\mathbf{x})$ and $b(\mathbf{x})$ over a set K is defined as

$$
(a; b)_K = \int_{\mathcal{B}} a(\mathbf{x}) \cdot b(\mathbf{x})\, \mathrm{d}K. \tag{30}
$$

the subscript will be dropped if $K = \Omega$. Herein, we employ the Galerkin formulation [74] for the energy equation and the Galerkin Gradient Least-Squares (GGLS) formulation for the diffusion-reaction equations [75].

3.1. Computational framework

The Galerkin weak form for the energy equations, Eqs. (3a)–(3d), can be written as follows: Find $\theta(\mathbf{x},\ t) \in \delta^t$ such that

$$(u;\ \rho c\dot{\theta}) + (\nabla u;\ \lambda\nabla\theta) + (u;\ \rho D\nabla c\cdot\nabla\theta) = -(u;\ \Delta H_k r_k) \quad \forall\, u(\mathbf{x}) \in \mathcal{U}. \tag{31}$$

franca and Durta Do Carmo [75] proposed the GGLS method which adds a term obtained by minimizing the square of the residual gradient to the Galerkin equation. The GGLS formulation for the species equations, Eqs. (4a)–(4d), reads as follows: Find $Y_i(\mathbf{x}, t) \in \mathcal{Y}_i^t$ such that

$$(v_i;\ \rho\dot{Y}_i) + (\nabla v_i;\ \rho D\nabla Y_i) + \sum_{e=1}^{N_e}\left(\nabla[\mathcal{F}(v_i)];\ \tau_{h_{\Omega_e}}\nabla[\mathcal{H}(Y_i)]\right)_{\Omega_e} = -(v_i;\ M_i r_k) \quad \forall\, v_i(\mathbf{x}) \in \mathcal{V}_i, \tag{32}$$

where N_e is the number of elements, h_{Ω_e} is the minimum element length, and

$$\mathcal{F} = \rho\frac{v_i}{\Delta t} + \nabla\cdot{}^{m}\mathbf{j}_i(v_i) + M_i r_k(v_i),$$
$$\mathcal{H} = \rho\dot{Y}_i + \nabla\cdot{}^{m}\mathbf{j}_i + M_i r_k, \tag{33}$$

where Δt is the time-step. The GGLS mesh-dependent parameter, $\tau_{h_{\Omega_e}}$, is defined as

$$\tau_{h_{\Omega_e}} = \frac{h_{\Omega_e}^2}{6M_i r_k}\,\xi_0(\mathbb{D}\mathrm{a}_h) \tag{34}$$

and

$$\xi_0(\chi) = \frac{\cosh(\chi)+2}{\cosh(\chi)-1} - \frac{6}{\chi^2}, \quad \mathbb{D}\mathrm{a}_h = \frac{M_i r_k h_{\Omega_e}^2}{\rho D}, \tag{35}$$

where $\mathbb{D}\mathrm{a}_h$ is the local (element) Damköhler number.

The finite elements considered for this study are the four-node quadrilateral elements. The nonlinear system of coupled equations, Eqs. (23) and (25), is iteratively solved using Newton's method. We implement a monolithic approach and a standard implicit Euler time integration which is first order accurate in time. The residuals and tangents are provided in Appendix B and verification studies to show the correctness of the implementation are presented in Appendix C.

4. Numerical results

This section presents numerical examples for the nonlinear chemo-thermal response of a Ni–Al premixed system as well as heterogeneous microstructures. In this work, we consider a simple particle system with no voids and micron-sized microstructural features (i.e., Ni and Al morphology). The microstructures are generated to have an average microstructural length-scale or feature size d_0 for Ni and Al. For this purpose, we use Karhunen–Loeve expansion to represent the microstructure as a realization from a Gaussian random field with zero mean and exponential covariance [51,76]. Figure 2 shows the microstructure with length-scale $d_0 = 5\,\mu$m.

The material properties and computational domain used in this section are provided in Table 1 and Fig. 3. Figure 3(a) shows a stoichiometric composition of Ni and Al with dimensions 1 mm by 0.1 mm. Figure 3(b) shows that the sample is heated, by applying a heat flux at the left boundary, to an approximate temperature ($\simeq$800 K) to locally initiate the kinetics. After 3 ms, the imposed heat flux at the boundary is removed to induce a self-sustained and self-propagating reaction. We define the temporal evolution of

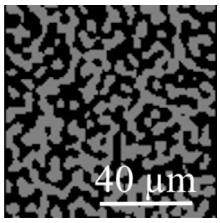

Fig. 2. Zoom of a generated microstructure with the average length-scale of 5 μm in 0.1 mm by 0.1 mm window shown in Fig. 3. The dark regions are Al and bright regions are Ni. The microstructures are generated to have the precise stoichiometric composition of Ni–Al.

quantities (temperature and mass fractions) by spatial averaging in the window shown in Figs. 2 and 3(a) as

$$\bar{\varphi}(t) = \frac{1}{\Omega}\int_{\Omega}\varphi(\mathbf{x}, t)\mathrm{d}\Omega. \tag{36}$$

In what follows, Section 4.1 presents sensitivity analysis and discusses calibration of reaction and diffusion parameters. Section 4.2 provides the detailed chemo-thermal responses of the Ni–Al system. Section 4.3 presents effect of the Ni–Al microstructures on temperature profile, flame speed, reaction time, and temperature increment during chemical reaction. Section 4.4 provides upscaling from the microstructural to the premixed problem using the multi-fidelity and multi-scale Gaussian Process (GP) emulator. Finally, animations of numerical simulations are provided in the Supplementary material.

4.1. Sensitivity analysis and Bayesian calibration of model parameters

We perform sensitivity analysis for the diffusion (D_0 and E_d) and reaction (A_k and E_k) parameters to study their effects on the variability of the average temperature throughout the simulation time. We also use the Bayesian inference to estimate the model parameters from set values of quantities of interest. In our work, the quantities of interest are the average maximum temperature ($\overline{\theta}_{\max}$), the average mass fraction of Al ($\overline{Y}_{\mathrm{Al}}$), and the average mass fraction of the product NiAl ($\overline{Y}_{\mathrm{NiAl}}$). These average values are calculated in the spatial window shown in Fig. 3 after reaction completion. The value for the maximum average temperature is based on the adiabatic flame temperature of the NiAl which is $\simeq$1911 K [13,77]. Furthermore, in the ideal conditions (e.g., neglecting boundary effects), the mass fractions of Al and NiAl should reach $\overline{Y}_{\mathrm{Al}} = 0.0$ and $\overline{Y}_{\mathrm{NiAl}} = 1.0$, which represents a status of full chemical convergence. In our Bayesian calibration, we use 5% uncertainty allowance for our quantities of interest of the average mass fraction of Al (i.e., $0.0 \le \overline{Y}_{\mathrm{Al}} \le 0.05$) and the product (i.e., $0.95 \le \overline{Y}_{\mathrm{NiAl}} \le 1.0$) at the end of the combustion process to account for non-ideal conditions (i.e., boundary effects, numerical inaccuracies, a surrogate for the quantities of interest). This leads to a faster convergence of the posteriors. Note however, that the mass balance is still strictly enforced: $Y_{\mathrm{Ni}} + Y_{\mathrm{Al}} + Y_{\mathrm{NiAl}} = 1$.

We use a microstructure with length-scale $d_0 = 10\,\mu$m and represent the model parameters by uniform random variables with ranges informed by the experimental studies. We note that native (i.e., not averaged) chemo-thermal material parameters for the solid state combustion synthesis are very difficult to measure and the literature provides a broad spectrum of values. For example, the measured range for the diffusion pre-exponent $(2.9 \pm 0.58) \times 10^{-12} \le D_0 \le (4.4 \pm 3.1) \times 10^{-4}$ [m^2/s] is from [62,78], the diffusion activation energy $45.4 \times 10^3 \le E_d \le (145.640 \pm 5.787) \times 10^3$ [J/mol] is from [62,79,80], and the kinetics activation energy $(17.4 \pm 2.85) \times 10^3 \le E_k \le (162.5 \pm 1.4) \times 10^3$ [J/mol] is from [81].

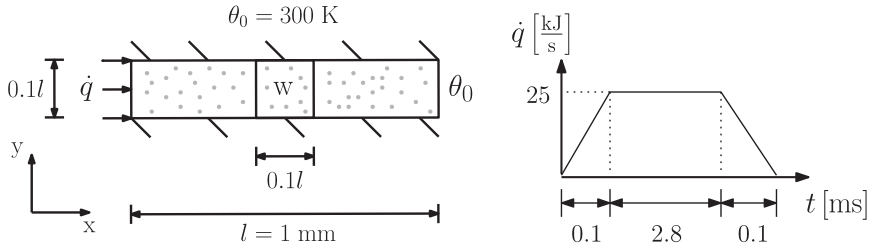

(a) Computational domain. (b) Heat flux at the boundary.

Fig. 3. (a) Computational domain with boundary conditions and the window in which averaged spatial quantities are evaluated (see Fig. 2). The domain is a 1 mm by 0.1 mm sample with the stoichiometric composition of Ni–Al. The top and bottom boundaries are insulated walls (i.e., zero heat flux). The right boundary is at constant prescribed temperature. (b) Heat flux profile at the left boundary.

Table 2
The ranges for the diffusion and reaction parameters.

Parameter	Range
D_0 [m^2/s]	$[1.0 - 2.0] \times 10^{-6}$
E_d/R [K]	$[5.5 - 7.5] \times 10^{+3}$
E_d [J/mol]	$[45.727 - 62.355] \times 10^{+3}$
A_k [m^3/(mol s)]	$[1.0 - 1.5]$
E_k/R [K]	$[3.3 - 3.8] \times 10^{+3}$
E_k [J/mol]	$[27.436 - 31.593] \times 10^{+3}$

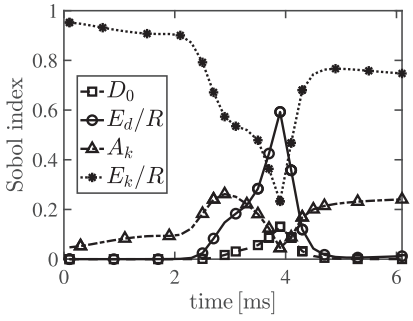

Fig. 4. The main Sobol' indices of the diffusion and reaction parameters. Throughout the combustion zone both the diffusion and reaction parameters play an essential role.

Because those ranges are too wide and to avoid computational difficulties, we perform sensitivity and calibration analyses using the model parameters with narrower ranges given in Table 2. These ranges are with lower activation energies as we target HEBM composites in this work. The range for A_k is obtained from numerical calibration runs such that the quantities of interest ($\overline{\theta}_{\max}$, $\overline{Y}_{\text{Al}}$, and $\overline{Y}_{\text{NiAl}}$) reach desired values with 5% uncertainty.

To estimate the contribution of each parameter to the global variance, we perform a variance-based sensitivity analysis (Sobol' indices) [82] as shown in Fig. 4. In the early simulation time (0–2.5 ms), when the chemical kinetics is initiating, the uncertainty in E_k/R is the most influential on the variance of the average temperature. In this stage, A_k has up to a 35% effect. During the intermediate simulation time (2.5–4.5 ms), when self-propagating reaction has formed, we observe a competition between diffusion and reaction in the reaction zone. This indicates that both diffusion and reaction are essential components of the chemo-thermal model of the NiAl system. In contrast to other models, where only diffusion is active [21,22,38], our model considers both diffusion and reaction. When approaching the end of the simulation time (4.5–6 ms), again the activation energy of reaction has the most influence on the variability of the average temperature. We note that the effect of diffusion is gradually diminished as the system becomes well mixed.

Table 3
The estimated mode, mean, standard deviation (std) and the coefficient of variation (cov) of the parameters using the posterior PDFs shown in Fig. 6.

Parameter	Mode	Mean	Std	Cov [%]
D_0 [m^2/s]	1.497×10^{-6}	1.511×10^{-6}	1.869×10^{-7}	12.531
E_d/R [K]	$6.151 \times 10^{+3}$	$6.179 \times 10^{+3}$	$0.242 \times 10^{+3}$	3.872
E_d [J/mol]	$51.139 \times 10^{+3}$	$51.372 \times 10^{+3}$	–	–
A_k [m^3/(mol s)]	1.341	1.372	0.059	4.528
E_k/R [K]	$3.550 \times 10^{+3}$	$3.542 \times 10^{+3}$	$0.061 \times 10^{+3}$	1.762
E_k [J/mol]	$29.515 \times 10^{+3}$	$29.448 \times 10^{+3}$	–	–

In the Bayesian framework, the prior knowledge of the parameters are updated to posterior using response from a computer model. The posterior Probability Density Function (PDF) $p(\kappa|s)$ of the model parameters is estimated using Bayes' rule as

$$p(\kappa|s) \propto p(\kappa)p(s|\kappa), \tag{37}$$

where $p(\kappa)$ and $p(s|\kappa)$ are the prior and the likelihood PDFs, respectively. Here, we denote the model parameters by the vector $\kappa = \{D_0, E_d/R, A_k, E_k/R\}$ and the data vector by $s = \{\overline{\theta}_{\max}, \overline{Y}_{\text{Al}}, \overline{Y}_{\text{NiAl}}\}$. We use uniform priors for the parameters with supports given in Table 2.

For independent and identically distributed Gaussian error between the data and model, the likelihood reads

$$p(s|\kappa) = \prod_{i=1}^{n} \frac{1}{\sigma\sqrt{2\pi}} \exp\left[-\frac{(s_i - \mathcal{M}(\kappa_i))^2}{2\sigma^2}\right], \tag{38}$$

where $\mathcal{M}(\kappa_i)$ denotes the model response for a given set of model parameters. In the Bayesian calibration procedure, it is a common practice to utilize a surrogate model in the likelihood in order to reduce the computational cost in estimating the posterior density [83]. To this end, we use Polynomial Chaos (PC) expansion [51,76] as a surrogate for the quantities of interest. The PC expansion can be expressed in a generic from as

$$\mathcal{M}(\kappa) = \sum_{i=0}^{P} m_i\phi_i, \qquad \text{where} \qquad m_i = \frac{\langle \mathcal{M}_i(\kappa)\phi_i \rangle}{\langle \phi_i^2 \rangle}. \tag{39}$$

Here, $\{\phi_i\}_{i=0}^{P}$ is a set of stochastic basis functions, and $<\bullet>$ denotes the expectation operator. To construct the PC surrogate, the uniform priors given in Table 2 are propagated through the computational model non-intrusively [82]. We use the second order Legendre polynomials for the stochastic basis functions [82]. Figure 5 shows the PDFs of $\overline{\theta}_{\max}$, and $\overline{Y}_{\text{NiAl}}$. These densities are generated from sampling the PC representation in Eq. (39). Having the priors and the likelihood, the posterior PDF given in Eq. (37) is estimated using a Markov Chain Monte Carlo (MCMC) sampling technique [84]. Figure 6 shows the estimated posterior as well as the prior PDFs of the model parameters. The posterior PDFs are unimodal with mode, mean, and standard deviation listed in Table 3. Note that all calibrated data are within the experimental intervals

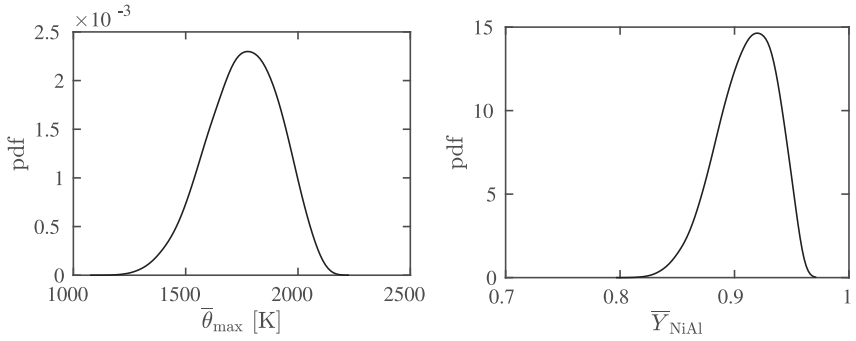

(a) Maximum average temperature. (b) Average mass fraction of NiAl.

Fig. 5. The PC surrogate PDFs of (a) the maximum average temperature and (b) the average mass fraction of NiAl.

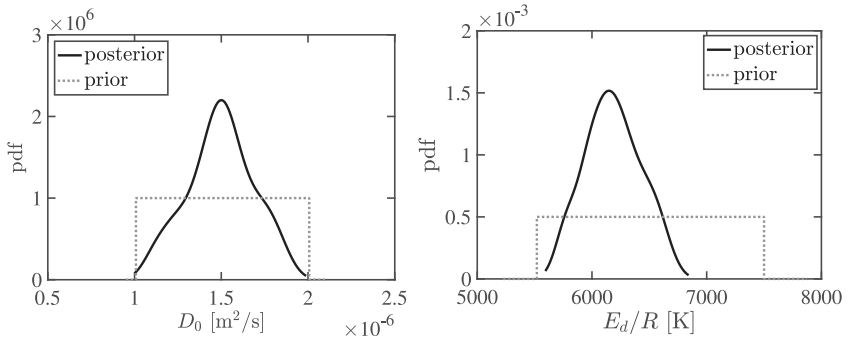

(a) Diffusion pre-exponent. (b) Diffusion activation energy over R.

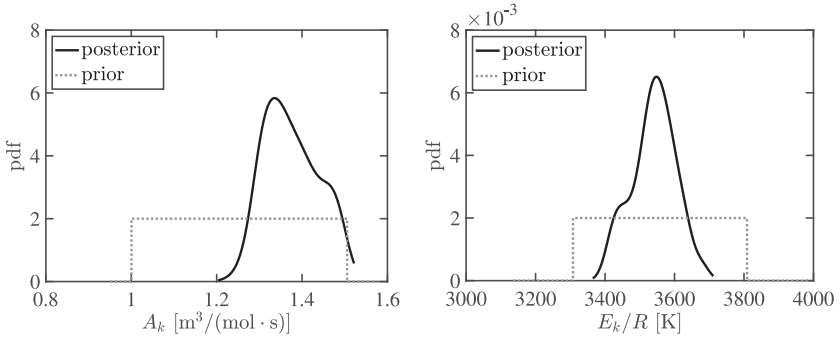

(c) Reaction pre-exponent. (d) Reaction activation energy over R.

Fig. 6. The prior and posterior PDFs of (a) the diffusion pre-exponent D_0, (b) the diffusion activation energy, E_d/R, (c) the reaction pre-exponent A_k, and (d) the reaction activation energy, E_k/R. We used 100,000 MCMC samples to estimate the posterior PDFs. Bayesian calibration is performed on a composite with microstructure, $d_0 = 10\,\mu$m.

discussed above. Moreover, because we target HEBM composites, our ranges are for lower activation energies.

To verify the order of the PC surrogate model and consequently the calibration results, we compare the results of the 2nd order PC with that of the 5th order PC expansion. The estimated mean of the model parameters using the 5th order PC and the corresponding errors are listed in Table 4. The relative error is defined as $e(\kappa_i) = \frac{||\kappa_i^{5th} - \kappa_i^{2nd}||_2}{||\kappa_i^{5th}||_2}$, where $\kappa_i \in \{D_0, E_d/R, A_k, E_k/R\}$. The relatively small magnitudes of the errors in the mean values of the parameters indicate that the 2nd order PC is sufficient as a surrogate model.

Table 4
The estimated mean of the parameters using 5th order (PC5) as a surrogate in the Bayesian analysis and the corresponding error between the 2nd order PC2.

Parameter	PC5	$e(\kappa_i)$
D_0 [m^2/s]	1.423×10^{-6}	6.341×10^{-2}
E_d/R [K]	$6.312 \times 10^{+3}$	2.110×10^{-2}
E_d [J/mol]	$52.477 \times 10^{+3}$	–
A_k [m^3/(mol s)]	1.310	4.582×10^{-2}
E_k/R [K]	$3.501 \times 10^{+3}$	1.141×10^{-2}
E_k [J/mol]	$29.107 \times 10^{+3}$	–

4.2. Chemo-thermal response

We now highlight the capabilities of the proposed model by providing detailed chemo-thermal responses of the Ni–Al system. In this section, we use the mean calibrated parameters in Table 3 and the computational domain in Fig. 3. At the beginning of this subsection, we provide spatial fields of temperature, species, and reaction rates and focus on both premixed and heterogeneous cases. For the heterogeneous cases, we study a simple

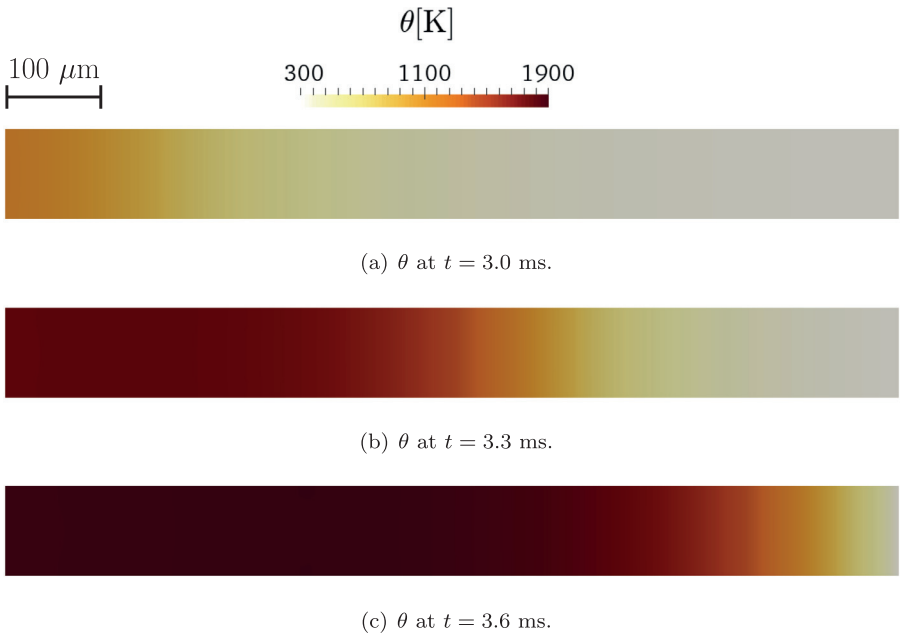

(a) θ at $t = 3.0$ ms.

(b) θ at $t = 3.3$ ms.

(c) θ at $t = 3.6$ ms.

Fig. 7. Temperature plots for the premixed problem. By applying the heat from the left boundary, the reaction initiates and the heat released from combustion increases the temperature to the adiabatic flame temperature of the Ni–Al reaction (≃1911 K).

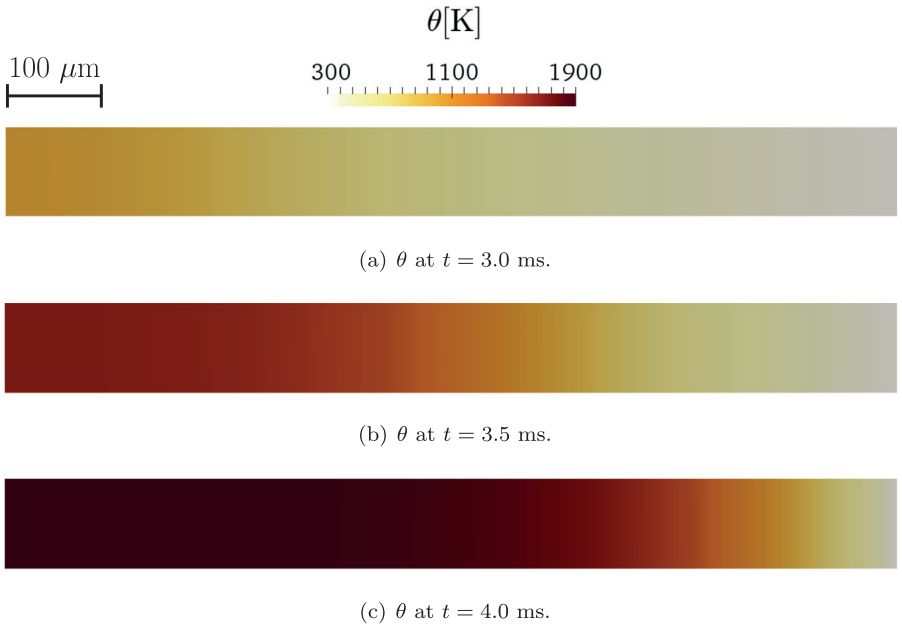

(a) θ at $t = 3.0$ ms.

(b) θ at $t = 3.5$ ms.

(c) θ at $t = 4.0$ ms.

Fig. 8. Temperature plots in the microstructure with $d_0 = 5\,\mu$m. The heat released from chemical reaction increases the temperature to the adiabatic flame temperature of the system.

one particle domain and assume no voids in the microstructure. This eliminates issues of particle-to-particle interactions [26,46]. In the subsection that follows, we look deeper into effects of the microstructural length-scale and provide comparisons and trends with existing experimental data.

Now, we first discuss results for the premixed case. The premixed system provides the limiting case with no microstructure (i.e., $d_0 \to 0$). Figure 7 shows the temperature at $t = 3.0$, 3.3, and 3.6 ms for a premixed system. The reaction is locally initiated at the left side of the sample by the heat flux shown in Fig. 3. After removing the applied flux, a self-propagating flame front forms and travels from left to right (Fig. 7(b) and (c)). As expected, the premixed case is the simplest to simulate, and based on the convergence study, we choose the mesh size of 10 μm with the time step of 10^{-4} s.

Next, we focus on the case with microstructure and show the temperature fields at $t = 3.0$, 3.5, and 4.0 ms for $d_0 = 5$ μm (see Fig. 8), and the mean values of parameters in Table 3. Similar to the premixed case, the initiated reaction at the left forms a self-propagating flame front (Fig. 8(b) and (c)). However, as expected and shown in Figs. 7(c) and 8(c), the high temperature front in the microstructure travels slower than in the premixed system. We will make a detailed comparison of the combustion wave speed in Section 4.3. For systems with microstructure, we have chosen the mesh size of 1 μm and the time step of 10^{-5} s (i.e., based on the convergence study).

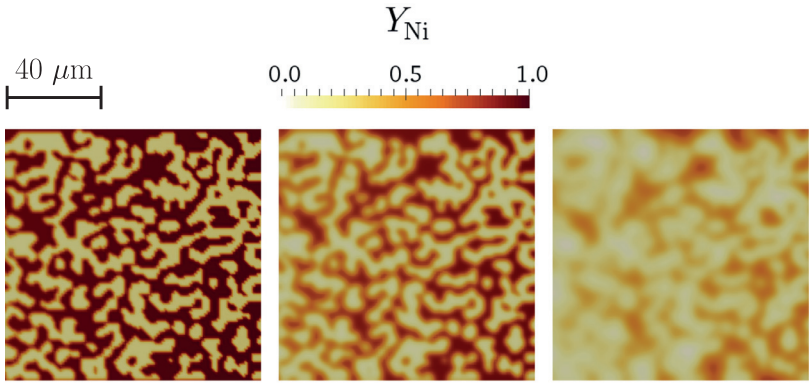

(a) Y_{Ni} at $t = 3.4$ ms. (b) Y_{Ni} at $t = 3.5$ ms. (c) Y_{Ni} at $t = 3.6$ ms.

Fig. 9. Mass fractions of Ni in the microstructure with $d_0 = 5\,\mu$m. (a), (b), and (c) depict the reaction front propagation through the window in higher detail.

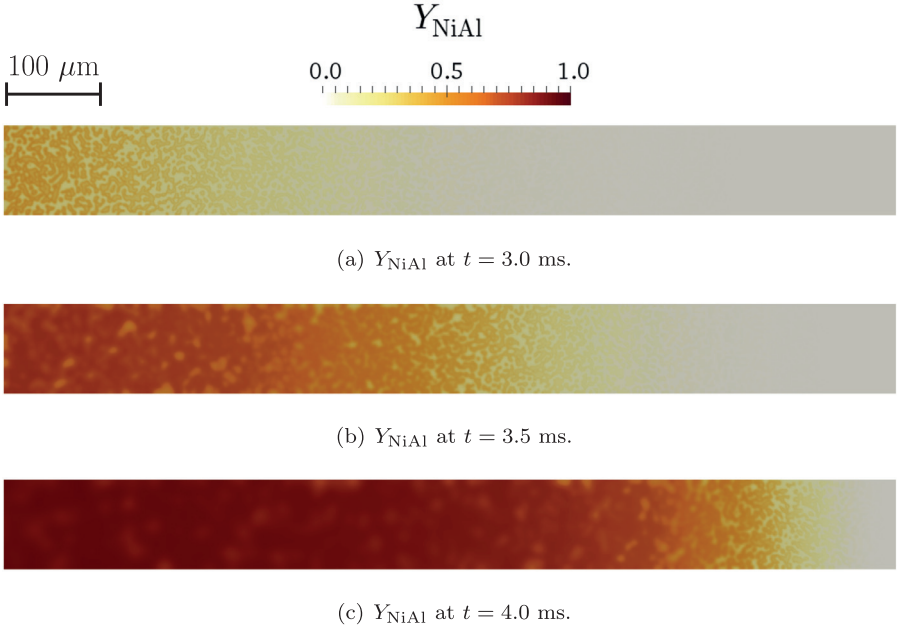

(a) Y_{NiAl} at $t = 3.0$ ms.

(b) Y_{NiAl} at $t = 3.5$ ms.

(c) Y_{NiAl} at $t = 4.0$ ms.

Fig. 10. Mass fractions of NiAl in the microstructure with $d_0 = 5\,\mu$m. (a) shows formation of NiAl. (b) and (c) show that on the left the reactants are converted to NiAl.

To highlight the complexity of the microstructure and conversion of species, we look at the mass fraction of Ni (Y_{Ni}) at $t = 3.4$, 3.5, and 3.6 ms, when the flame front reaches the middle window (see Fig. 3). These results are depicted in Fig. 9(a)–(c). As one can see, Ni gets progressively consumed during the solid state combustion synthesis. Results for Al are similar (dual opposites) to those of Ni and are not displayed for brevity. The formation of the product (NiAl) in the microstructure is presented in Fig. 10. As the flame front passes the microstructure, Ni and Al are converted to NiAl.

To investigate the effect of the microstructure on the chemical reaction, the reaction rates are plotted in Fig. 11. The detailed results for the reaction rates in the simulation window (see Fig. 3) are shown in Fig. 12. One can see the complex spatial reaction profile, with the highest reaction rates occurring at the interfaces between the constituents. This highlights the impact of the microstructure and the effect of the contact area between constituents, which is absent in the fully premixed case [24].

4.3. Effect of microstructure on reaction process

In this section, we study the effect of microstructures on the Ni–Al system by using the mean calibrated parameters in Table 3 and the computational domain in Fig. 3. The numerical results are for three sets of 25 samples with the average Ni and Al length-scale $d_0 = 5$, 10, and 15 m. We address the time profiles for spatially averaged temperature and mass fraction of NiAl, Eq. (36), and the associated uncertainties due to the microstructures.

Figure 13 shows the temporal evolution of average temperature ($\overline{\theta}$) and product mass fraction ($\overline{Y}_{\mathrm{NiAl}}$) bounded by 95% confidence intervals chosen in the calibration study in Section 4.1. The profiles show that for the finer microstructures the reaction occurs sooner and propagates faster. Figure 13(a) shows that $\overline{\theta}$ for all samples increases to the adiabatic flame temperature of Ni–Al reaction ($\simeq$1911 K). The decay in the temperature profile is due to the finite length of the sample, and applied temperature ($\theta_0 = 300$ K) at the right boundary (see Fig. 3(a)). As expected, chemical conversion to NiAl occurs earlier for the finer microstructures in Fig. 13(b). Note that Fig. 13(b) shows the spatial average in the selected window (Fig. 3). Locally, our model achieves full conversion in a large portion of the window, but the complex microstructure and non-ideal conditions lead to a few percent of the unconsumed reactants as $\overline{Y}_{\mathrm{NiAl}} \to 1$ on average.

Figure 14 shows the average flame speed and reaction time with associated uncertainties (95% confidence interval from 25 microstructures) in the selected window. Because we consider

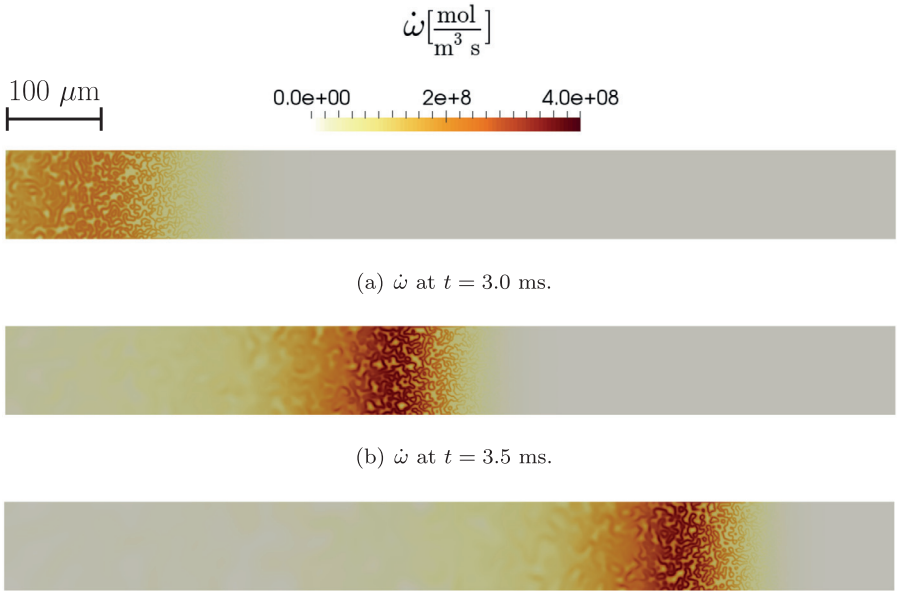

(a) $\dot{\omega}$ at $t = 3.0$ ms.

(b) $\dot{\omega}$ at $t = 3.5$ ms.

(c) $\dot{\omega}$ at $t = 4.0$ ms.

Fig. 11. Reaction rates in the microstructure with $d_0 = 5\,\mu$m. (a) shows that by applying the heat flux at the left boundary, the reaction initiates locally and becomes self-sustained. (b) and (c) show the reaction zones and propagation of the reaction rates through the cell.

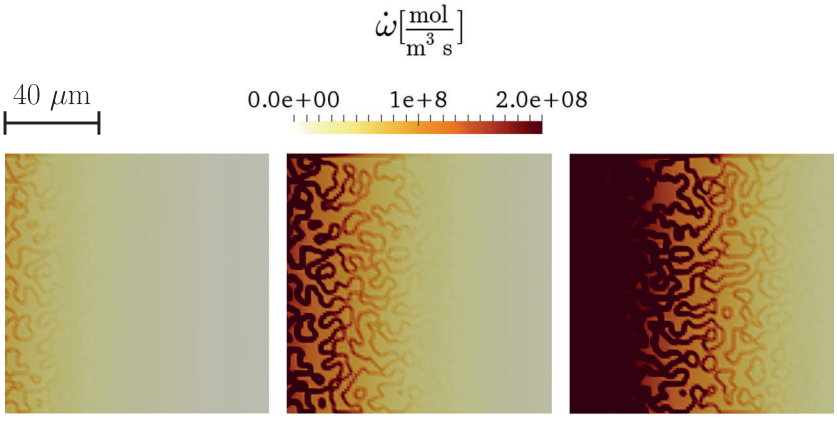

(a) $\dot{\omega}$ at $t = 3.3$ ms. (b) $\dot{\omega}$ at $t = 3.4$ ms. (c) $\dot{\omega}$ at $t = 3.5$ ms.

Fig. 12. Reaction rates in the microstructure with $d_0 = 5\,\mu$m. (a), (b), and (c) show the rate propagation in the selected window in higher detail.

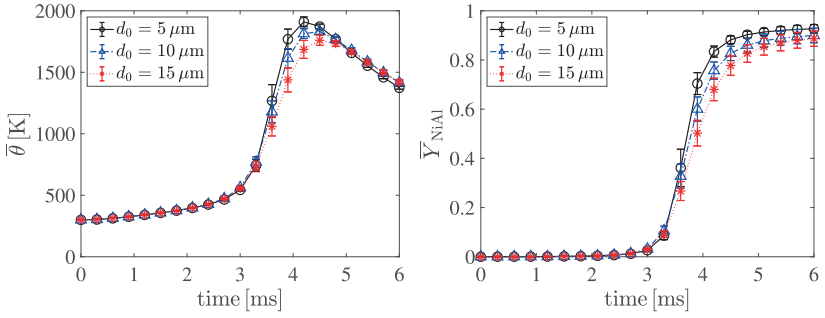

(a) Average temperature. (b) Average product mass fraction.

Fig. 13. Effect of microstructures on the spatially averaged temperature and mass fraction. The results are evaluated in the selected window (Fig. 3). The error bars represent 95% confidence interval for 25 microstructural samples. (a) and (b) show that for the finer length-scale, the reaction occurs sooner, propagates faster, and conversion to NiAl occurs earlier.

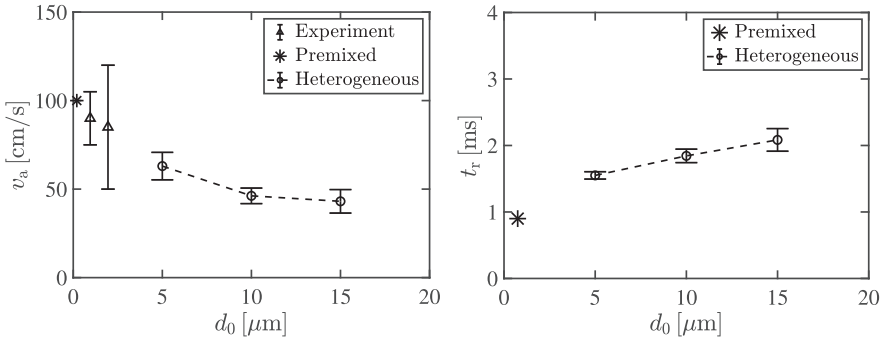

(a) Average speed. (b) Average reaction time.

Fig. 14. Effect of the microstructure on the average flame speed and the reaction time for the premixed case and system with the microstructure. The results are evaluated in the selected window (Fig. 3). (a) shows the average speed of flame propagation. (b) depicts reaction times. The error bars represent 95% confidence interval for 25 microstructural samples. The experimental data is adapted from [26] where d_0 is the length-scale of Al.

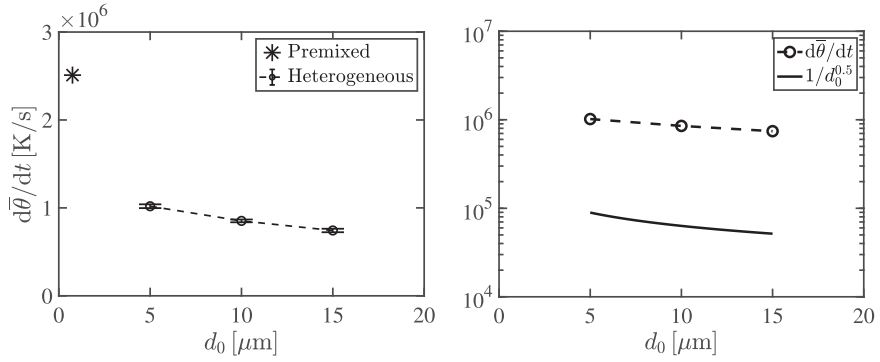

(a) Average time-temperature slope. (b) Scaling between slope and d_0.

Fig. 15. Slope of temporal evolution of average temperatures for the premixed case and microstructures. (a) shows that for the finer microstructures, we have a greater temperature-time slope. The error bars represent 95% confidence interval for 25 microstructural samples. (b) depicts scaling expression between the length-scale d_0 and time-temperature profile.

only one heterogeneous particle with no voids, there is no hesitation time during the reaction propagation between particles as discussed in [26,46]. Thus, our average velocity is identical to the instantaneous velocity in those studies. The experimental instantaneous velocity for systems with Al length-scale $\simeq 2\,\mu$m and Ni length-scale $\simeq 10\,\mu$m is $v_a \geq 80 \pm 35$ cm/s [26,46]. Similarly to experimental findings, our computational results show that the average speed of flame propagation is faster for finer microstructures and reaction time is shorter. Figure 14 also shows the average flame speed and reaction time for the premixed case (i.e., $d_0 \to 0$). The computed velocities from our work (i.e., both the premixed system and microstructural cases) follow the trend of the experimental instantaneous velocities reasonably well. Detailed simulations with finer microstructures are needed to close the gap for validation.

Figure 15 depicts the computed time-temperature slope with associated uncertainties (95% confidence interval for 25 samples) in the selected window. As expected for the finer microstructure, we observed a sharper temperature slope. The slope of temperature profiles has the same order of magnitude as in [85,86] which is $\simeq 10^5 - 10^6$ K/s. We also provide the slope for the premixed case which is $\geq 10^6$ K/s. Moreover, we relate the microstructural scale to the dynamics of chemical kinetics [87]. In particular, we found a scaling expression between the slope of the temperature profile and length-scale d_0 as

$$\frac{\mathrm{d}\bar{\theta}}{\mathrm{d}t} \sim \frac{1}{d_0^n}. \tag{40}$$

Figure 15 depicts this scaling expression for exponent $n = 1/2$.

4.4. Multi-fidelity and multi-scale emulator

The computational cost of detailed simulations on heterogeneous composites increases rapidly as the length-scale, d_0, of the microstructure decreases. However, simulations on a premixed domain are scale-independent and thus inexpensive to execute compared to the heterogeneous case. This fact motivates us to develop a Multi-Fidelity and Multi-Scale Gaussian Process emulator (MFMS-E) to overcome the computational cost of simulations at different length-scales. The emulator is constructed in two steps. First, we utilize a small number of runs using a heterogeneous domain for a given length-scale (i.e., d_0-fixed) and a large number of runs on a premixed domain to construct a multi-fidelity Gaussian Process (GP). The material parameters used for these runs are sampled from the posterior PDFs shown in Fig 6. In the second step, we generate realizations from the multi-fidelity GP at different length-scales, d_0, to build the multi-scale GP.

In particular, for length-scales ($d_0 = 5, \ldots, 15$), we define a high-fidelity statistical model (representing the heterogeneous case) as a linear combination of a low-fidelity model (representing the premixed case) and a model discrepancy as [52,53]

$$\mathcal{Y}^H_{d_0}(\kappa, t) = \gamma_{d_0}\mathcal{Y}^L(\kappa, t) + \zeta_{d_0}(t), \quad \text{for } d_0 = 5, \ldots, 15, \tag{41}$$

where $\mathcal{Y}^H_{d_0}(\kappa, t)$ and $\mathcal{Y}^L(\kappa, t)$ are the outputs of the high-fidelity (heterogeneous) model and the low-fidelity (premixed) model. The parameter γ_{d_0} represents a correlation coefficient and $\zeta_{d_0}(t)$ denotes the discrepancy between the high and low fidelity models. The outputs of the low fidelity model as well as the discrepancy term are represented as realizations from a GP with zero mean

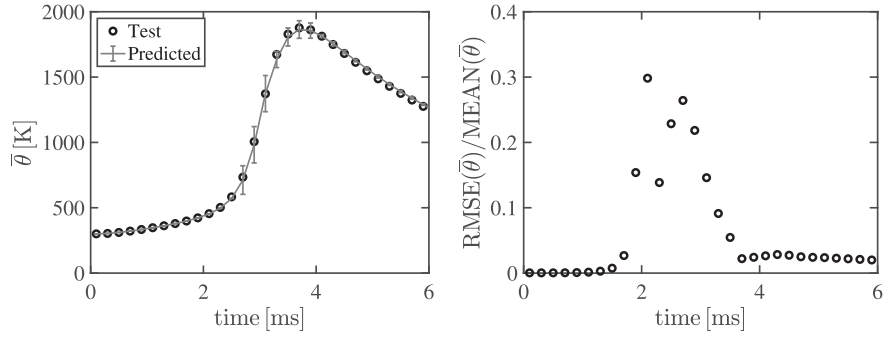

(a) Average temperature. (b) Normalized root mean squared error.

Fig. 16. Verification of the multi-fidelity GP. (a) The prediction of the multi-fidelity GP is verified against the output of the heterogeneous case for given material parameters. The relative L_2 norm of the error is 1.04×10^{-2}. (b) The normalized root mean squared error of the GP predictions using 5 different sets of the model parameters.

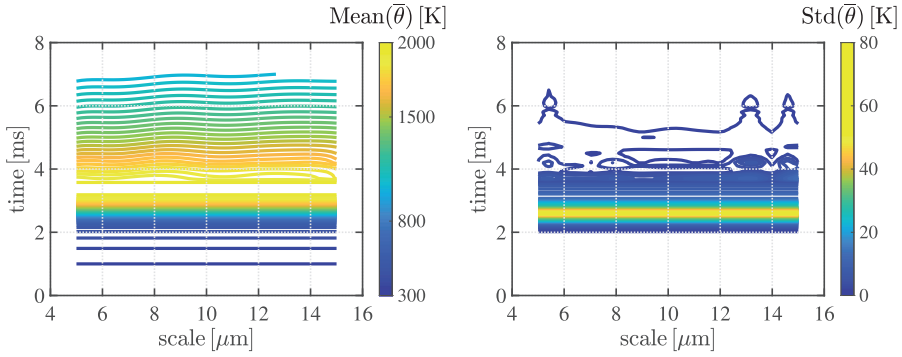

(a) Mean. (b) Standard deviation.

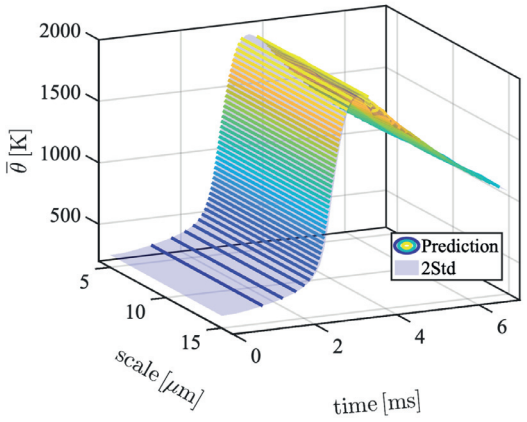

(c) Mean and lower bound of 95% confidence interval.

Fig. 17. The prediction mean and the standard deviation of the MFMS-E for the average temperature. (a) Contour lines of the mean across time and the length-scale. (b) Contour lines of the standard deviation across time and the length-scale. (c) 3D visualization of the prediction mean and the lower bound of the 95% confidence interval (i.e., mean $\pm$ 2Std).

and squared exponential covariance functions as $\mathcal{Y}^L \sim \mathcal{GP}(0, K^L)$ and $\zeta_{d_0} \sim \mathcal{GP}(0, K^D)$, respectively [88,89]. Thus, the joint distribution of the low and high fidelity outputs can be expressed as

$$\begin{bmatrix} \mathcal{Y}^L \\ \mathcal{Y}^H_{d_0} \end{bmatrix} \sim \mathcal{GP}\left(0, \begin{bmatrix} K^L & \gamma_{d_0} K^L \\ \gamma_{d_0} K^L & \gamma_{d_0}^2 K^L + K^D \end{bmatrix}\right). \tag{42}$$

The hyper-parameters of both the low-fidelity and discrepancy covariance functions are estimated using Maximum Likelihood Estimation (MLE) at each time step [88,89].

For the numerical results, we use 50 runs on a premixed domain and 5 runs on a heterogeneous domain to construct the multi-fidelity GP for a given length-scale. We verify the prediction of the multi-fidelity GP against the output of the high-fidelity model as shown in Fig. 16. The relative norm of the error is $e(X) = \frac{||\bar{\theta}_{d_0} - \bar{\theta}_p||_2}{||\bar{\theta}_p||_2} = 1.04 \times 10^{-2}$. The normalized root mean squared error is calculated based on 5 realizations of the model parameters yielding a maximum value less than $\frac{\text{RMSE}(\bar{\theta})}{\text{MEAN}(\bar{\theta})} = 0.4$ within the combustion zone.

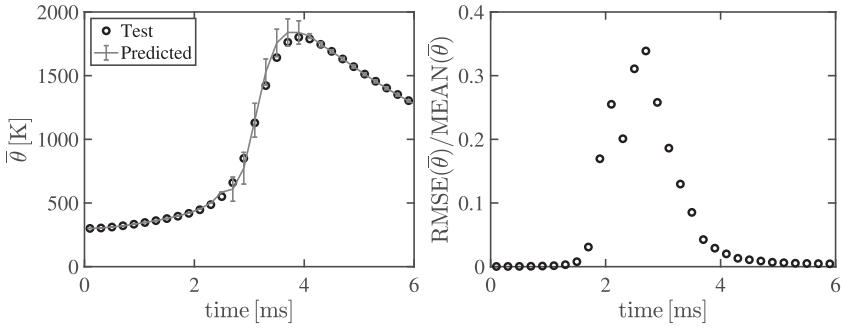

(a) Average temperature. (b) Normalized root mean squared error.

Fig. 18. Verification of the MFMS-E. (a) The prediction of the MFMS-E is verified against the output of the heterogeneous case with length-scale $d_0 = 13\,\mu$m. The relative L_2 norm of the error is 3.54×10^{-2}. (b) The normalized root mean squared error of the MFMS-E prediction using 10 different sets of the parameters.

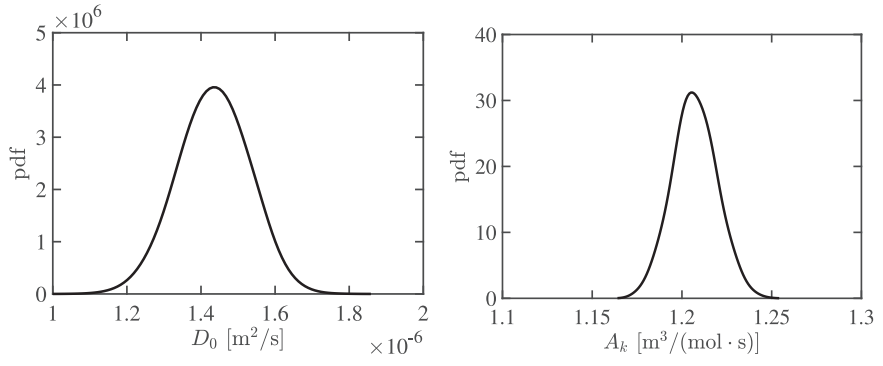

(a) Diffusion pre-exponent. (b) Reaction pre-exponent.

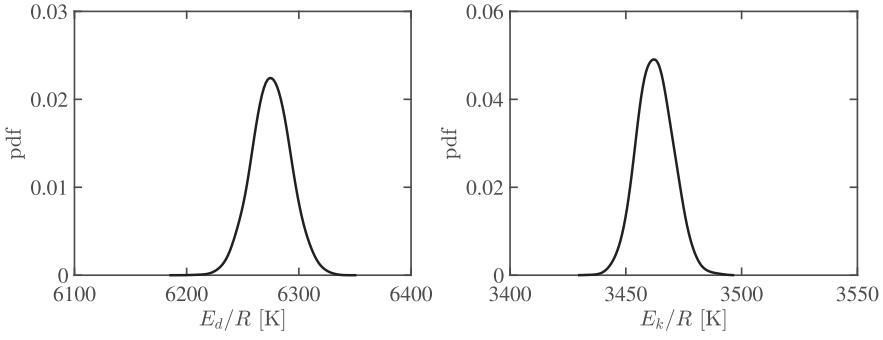

(c) Diffusion activation energy over R. (d) Reaction activation energy over R.

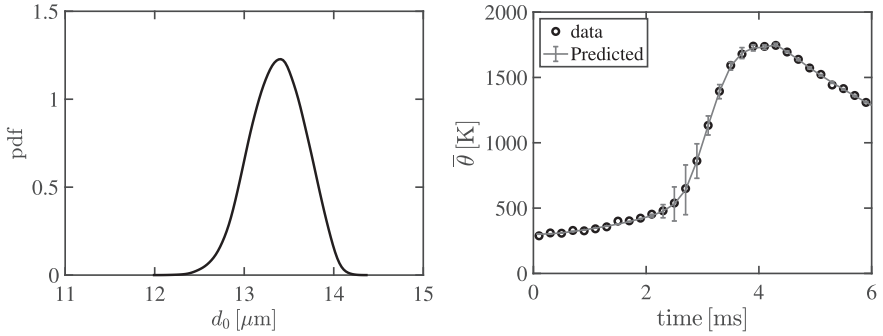

(e) length-scale. (f) Prediction of the MFMS-E.

Fig. 19. The posterior PDFs and the prediction of the MFMS-E. (a) Posterior PDF of the diffusion pre-exponent D_0, (b) Posterior PDF of the reaction pre-exponent A_k, (c) Posterior PDF of the diffusion activation energy, E_d/R, (d) Posterior PDF of the reaction activation energy, E_k/R. (e) Posterior PDF of the length-scale d_0, (f) The prediction of the MFMS-E and the noisy synthesized measurement data.

Table 5
The true and estimated values of the model parameters with the corresponding L_2 norm of the difference. The true parameters are used to synthesize the measurement in Fig. 19(f) and the estimated mean values are from Bayesian inversion using the MFMS-E.

Parameter	True value	Estimated value	$e(X)$
d_0 [μm]	13.000	13.369	2.771×10^{-2}
D_0 [m^2/s]	1.450×10^{-6}	1.434×10^{-6}	1.119×10^{-2}
E_d/R [K]	$6.278 \times 10^{+3}$	$6.275 \times 10^{+3}$	0.102×10^{-2}
E_d [J/mol]	$52.198 \times 10^{+3}$	$52.173 \times 10^{+3}$	–
A_k [$m^3/(mol\,s)$]	1.200	1.211	0.802×10^{-2}
E_k/R [K]	$3.450 \times 10^{+3}$	$3.457 \times 10^{+3}$	0.199×10^{-2}
E_k [J/mol]	$28.685 \times 10^{+3}$	$28.743 \times 10^{+3}$	–

Next, we generate 10 realizations from the multi-fidelity GP at each length-scale ($d_0 = 5, 6, 7, 9, 10, 11, 12, 14, 15\,\mu m$). These realizations are inexpensive and easy to generate. We use these realizations to build the coupling mechanism across the length-scale. Note that we randomly select length-scales (8 and 13 μm) for later verification. For the multi-scale emulator, we use a GP with zero mean and squared exponential covariance function. The hyper-parameters of the covariance function are also estimated using MLE. Note that in this step, the length-scale is treated as a parameter in constructing the GP.

For a given set of model parameters, Fig. 17 shows the mean and standard deviation (std) of the average temperature distribution across the time and length-scale. Figure 18 shows the verification results and the normalized root mean squared error for 13 μm length-scale. The relative norm of the error is $e(\bar{\theta}) = \frac{||\bar{\theta}_{d_0} - \bar{\theta}_p||_2}{||\bar{\theta}_p||_2} = 3.54 \times 10^{-2}$ and the maximum value of the normalized root mean squared error is less than $\frac{\text{RMSE}(\bar{\theta})}{\text{MEAN}(\bar{\theta})} = 0.4$ within the combustion zone. Note that the model parameters and the length-scale used for the verification were not in the database used to construct the emulator.

4.5. Bayesian inversion discovery

In this section, we use the MFMS-E within the Bayesian framework to infer the length-scale as well as parameters from a synthesized noisy measurement data of the average temperature profile. Here, we use the same likelihood function given in Eq. (38). However, now the data vector, s, is a synthesized noisy measurement of the average temperature and we substitute the MFMS-E for the surrogate $\mathcal{M}(\kappa_i)$. The posterior PDFs of the length-scale and the parameters are shown in Fig. 19(a)–(e). Table 5 lists the values used to generate the virtual measurement and the estimated mean values. Note that the length-scale and the parameters used to generate the virtual measurement are not in the database used to construct the MFMS-E. This shows the robustness of the emulator. Figure 19(f) shows the prediction of the MFMS-E using the estimated mean values of the length-scale and parameters listed in Table 5 in conjunction with the synthesized measurement of the average temperature profile. The prediction from MFMS-E agrees reasonably well with the virtual measurement of the average temperature profile as expected because of the small differences in the estimation of the parameters as shown in Table 5.

5. Conclusions

We have developed a two-way coupled chemo-thermal model and implemented it within a finite element framework to simulate combustion synthesis of NiAl composites. We show that the model satisfies the second law of thermodynamics. We consider both diffusion and reaction in the provided model and used nonlinear Arrhenius type diffusion and reaction equations. Rigorous sensitivity analysis is performed to show the effect of the reaction and diffusion phenomena on the synthesis process. We observed that in the combustion zone both the reaction and diffusion play an important role. The influence of the microstructure on the behavior of the system was also investigated, and detailed simulation results, average chemical front speed, reaction time, and slope of temperature-time profile were provided. Additionally, we developed a multi-fidelity and multi-scale Gaussian process emulator to overcome the computational costs associated with simulations at different length-scales. The emulator is used within a Bayesian framework to estimate the parameters and the underlying length-scale of the microstructure from a synthesized measurement of the temperature profile.

The emphasis of this work has been on the development of a mathematical and computational model for self-propagating material synthesis. We consider solid state reaction process and study micron-sized single particle systems with no voids. Numerical simulations of finer material systems (i.e., $d_0 \leq 1.0\,\mu m$) or systems with more complex reaction mechanisms (i.e., intermediate phases) are important future topics.

Conflict of interest

None.

Acknowledgments

This work was supported by the Department of Energy, National Nuclear Security Administration, under the Award No. DE-NA0002377 as part of the Predictive Science Academic Alliance Program II.

Appendix A. Dissipation inequalities

Herein, we show that the proposed chemo-thermal model satisfies the second law of thermodynamics. We rearrange the first law for the entropy, and show that the heat, mass diffusion, and chemical dissipation inequalities obey the second law.

Substitute Eq. (2) for $\dot{e}$, Eq. (16) for $\dot{\psi}$, and Eq. (4a) for $\dot{Y}_i$ into Eq. (13) and simplify to get

$$\rho\dot{\eta} = -\frac{1}{\theta}\nabla\cdot{}^{\mathrm{q}}\mathbf{j} + \frac{1}{\theta}\sum_{i=1}^{N_s}\mu_i\nabla\cdot{}^{\mathrm{m}}\mathbf{j}_i - \frac{1}{\theta}\sum_{i=1}^{N_s}M_i\mu_i\dot{\omega}_i. \tag{43}$$

one can rearrange Eq. (43) to get

$$\begin{aligned}\rho\dot{\eta} &= -\nabla\cdot\left(\frac{{}^{\mathrm{q}}\mathbf{j}}{\theta}\right) - \frac{1}{\theta^2}{}^{\mathrm{q}}\mathbf{j}\cdot\nabla\theta \\ &\quad - \sum_{i=1}^{N_s}\left(\nabla\left(\frac{\mu_i}{\theta}\right)\cdot{}^{\mathrm{m}}\mathbf{j}_i - \nabla\cdot\left(\frac{\mu_i}{\theta}{}^{\mathrm{m}}\mathbf{j}_i\right) - \frac{1}{\theta}M_i\mu_i\dot{\omega}_i\right), \\ &= -\nabla\cdot\left(\frac{{}^{\mathrm{q}}\mathbf{j}}{\theta} - \frac{1}{\theta}\sum_{i=1}^{N_s}\mu_i{}^{\mathrm{m}}\mathbf{j}_i\right) - \frac{1}{\theta^2}{}^{\mathrm{q}}\mathbf{j}\cdot\nabla\theta \\ &\quad - \sum_{i=1}^{N_s}\nabla\left(\frac{\mu_i}{\theta}\right)\cdot{}^{\mathrm{m}}\mathbf{j}_i - \frac{1}{\theta}\sum_{i=1}^{N_s}M_i\mu_i\dot{\omega}_i.\end{aligned}$$

next, we define the entropy flux per unit area, ${}^{\eta}\mathbf{j}$, and the entropy production per unit volume, σ, as [63]

$${}^{\eta}\mathbf{j} = -\frac{{}^{\mathrm{q}}\mathbf{j}}{\theta} + \frac{1}{\theta}\sum_{i=1}^{N_s}\mu_i{}^{\mathrm{m}}\mathbf{j}_i, \tag{44}$$

$$\sigma = -\frac{1}{\theta^2}{}^{\mathrm{q}}\mathbf{j}\cdot\nabla\theta - \sum_{i=1}^{N_s}\nabla\left(\frac{\mu_i}{\theta}\right)\cdot{}^{\mathrm{m}}\mathbf{j}_i - \frac{1}{\theta}\sum_{i=1}^{N_s}M_i\mu_i\dot{\omega}_i. \tag{45}$$

now, the first law can be rewritten in the following form [63]

$$\rho\dot{\eta} = \nabla\cdot{}^{\eta}\mathbf{j} + \sigma, \tag{46}$$

$$\sigma \geq 0. \tag{47}$$

note that σ is the entropy generation due to the energy flux, mass diffusion, and chemical reaction. One can expand σ to get

$$-\frac{1}{\theta^2}{}^{\mathrm{q}}\mathbf{j}\cdot\nabla\theta-\frac{1}{\theta}\sum_{i=1}^{N_s}\nabla\mu_i\cdot{}^{\mathrm{m}}\mathbf{j}_i+\frac{1}{\theta^2}\sum_{i=1}^{N_s}\mu_i\nabla\theta\cdot{}^{\mathrm{m}}\mathbf{j}_i$$
$$-\frac{1}{\theta}\sum_{i=1}^{N_s}M_i\mu_i\dot{\omega}_i\geq 0. \tag{48}$$

substituting ${}^{\mathrm{q}}\mathbf{j}$ from Eq. (8) gives

$$-\frac{1}{\theta^2}\left(\mathbf{q}+\sum_{i=1}^{N_s}h_i{}^{\mathrm{m}}\mathbf{j}_i\right)\cdot\nabla\theta-\frac{1}{\theta}\sum_{i=1}^{N_s}\nabla\mu_i\cdot{}^{\mathrm{m}}\mathbf{j}_i+\frac{1}{\theta^2}\sum_{i=1}^{N_s}\mu_i\nabla\theta\cdot{}^{\mathrm{m}}\mathbf{j}_i$$
$$-\frac{1}{\theta}\sum_{i=1}^{N_s}M_i\mu_i\dot{\omega}_i\geq 0. \tag{49}$$

using $\mu_i=h_i-\eta_i\theta$, we obtain

$$-\frac{1}{\theta^2}\mathbf{q}\cdot\nabla\theta-\frac{1}{\theta}\sum_{i=1}^{N_s}\nabla\mu_i\cdot{}^{\mathrm{m}}\mathbf{j}_i-\frac{1}{\theta}\sum_{i=1}^{N_s}\eta_i\nabla\theta\cdot{}^{\mathrm{m}}\mathbf{j}_i$$
$$-\frac{1}{\theta}\sum_{i=1}^{N_s}M_i\mu_i\dot{\omega}_i\geq 0, \tag{50a}$$

$$-\frac{1}{\theta^2}\mathbf{q}\cdot\nabla\theta-\frac{1}{\theta}\sum_{i=1}^{N_s}(\nabla\mu_i+\eta_i\nabla\theta)\cdot{}^{\mathrm{m}}\mathbf{j}_i-\frac{1}{\theta}\sum_{i=1}^{N_s}M_i\mu_i\dot{\omega}_i\geq 0. \tag{50b}$$

Now, we present a strong form of the second law and define the heat, mass diffusion, and chemical dissipation inequalities as

$${}^{\mathrm{q}}\mathcal{D}=-\frac{1}{\theta^2}\mathbf{q}\cdot\nabla\theta\geq 0, \tag{51a}$$

$${}^{\mathrm{m}}\mathcal{D}=-\frac{1}{\theta}\sum_{i=1}^{N_s}(\nabla\mu_i+\eta_i\nabla\theta)\cdot{}^{\mathrm{m}}\mathbf{j}_i\geq 0, \tag{51b}$$

$${}^{\mathrm{c}}\mathcal{D}=-\frac{1}{\theta}\sum_{i=1}^{N_s}M_i\mu_i\dot{\omega}_i\geq 0. \tag{51c}$$

recalling that heat conduction $\mathbf{q}=-\lambda\Delta\theta$ and $\lambda\geq 0$, we get

$${}^{\mathrm{q}}\mathcal{D}=\frac{\lambda}{\theta^2}\nabla\theta\cdot\nabla\theta\geq 0. \tag{52}$$

therefore, the heat dissipation inequality, ${}^{\mathrm{q}}\mathcal{D}$, is positive semidefinite and satisfies the second law.
for mass diffusion dissipation ${}^{\mathrm{m}}\mathcal{D}$ in Eq. (51b), one can write

$${}^{\mathrm{m}}\mathcal{D}=-\frac{1}{\theta}\sum_{i=1}^{N_s}(\nabla\overline{\mu}_i+\overline{\eta}_i\nabla\theta)\cdot{}^{\mathrm{m}}\bar{\mathbf{j}}_i, \tag{53}$$

where $\overline{\mu}_i=M_i\mu_i$, $\overline{\eta}_i=M_i\eta_i$, ${}^{\mathrm{m}}\bar{\mathbf{j}}_i={}^{\mathrm{m}}\mathbf{j}_i/M_i=-\overline{\rho}D\nabla y_i$, and $\overline{\rho}=\rho/M$ is the mixture molar density. Here, $y_i=MY_i/M_i$ are the species mole fractions. In our definition of ${}^{\mathrm{m}}\bar{\mathbf{j}}_i$, we have made the approximation that the mixture molecular mass, M, is well-modeled as a constant. Recalling $\overline{\mu}_i=\overline{h}_i-\overline{\eta}_i\theta$ and using definitions of enthalpy and entropy from Eqs. (6a) and (6b), one gets

$$\begin{aligned}\nabla\overline{\mu}_i+\overline{\eta}_i\nabla\theta&=\nabla\overline{h}_i-\theta\nabla\overline{\eta}_i,\\&=M_ic_i\nabla\theta-M_i\theta\left(c_i\frac{\nabla\theta}{\theta}-\frac{R}{M_i}\frac{\nabla y_i}{y_i}\right),\\&=R\theta\frac{\nabla y_i}{y_i},\end{aligned} \tag{54}$$

where $\overline{h}_i=M_ih_i$. Now, after substituting Eq. (54) and ${}^{\mathrm{m}}\bar{\mathbf{j}}_i$ into Eq. (53), we obtain

$${}^{\mathrm{m}}\mathcal{D}=\overline{\rho}RD\sum_{i=1}^{N_s}\frac{\nabla y_i\cdot\nabla y_i}{y_i}\geq 0. \tag{55}$$

because $\overline{\rho}>0$, $R>0$, $D\geq 0$, and $y_i\geq 0$, one sees that the dissipation inequality of mass diffusion is positive semidefinite and it satisfies the second law.

For the chemical dissipation ${}^{\mathrm{c}}\mathcal{D}$, one can substitute Eq. (12b) to get

$${}^{\mathrm{c}}\mathcal{D}=-\frac{1}{\theta}\sum_{i=1}^{N_s}M_i\mu_i\sum_{k=1}^{N_r}\nu_{ik}r_k. \tag{56}$$

we define the chemical affinity $\overline{\alpha}_k$ for the kth reaction [56]

$$\overline{\alpha}_k=-\sum_{i=1}^{N_s}M_i\mu_i\nu_{ik}=R\theta\ln\left[\frac{\mathcal{R}'_k}{\mathcal{R}''_k}\right], \tag{57}$$

where $\nu_{ik}=\nu''_{ik}-\nu'_{ik}$ and the forward and backward reaction coefficients are

$$\mathcal{R}'_k=k_k\prod_{j=1}^{N_s}\left(\frac{\rho Y_j}{M_j}\right)^{\nu'_{jk}}, \tag{58a}$$

$$\mathcal{R}''_k=\frac{k_k}{K_{\mathrm{eq}_k}}\prod_{j=1}^{N_s}\left(\frac{\rho Y_j}{M_j}\right)^{\nu''_{jk}}. \tag{58b}$$

here, $r_k=\mathcal{R}'_k-\mathcal{R}''_k$ in Eq. (12b). Substituting Eqs. (57) and (58) into Eq. (56) gives

$${}^{\mathrm{c}}\mathcal{D}=R\sum_{k=1}^{N_r}\ln\left[\frac{\mathcal{R}'_k}{\mathcal{R}''_k}\right]\left(\mathcal{R}'_k-\mathcal{R}''_k\right)\geq 0. \tag{59}$$

here, $k_k(\theta)>0$, $K_{\mathrm{eq}_k}(\theta)=\exp[\frac{-\Delta G^0_k}{R\theta}]>0$, and $R>0$, enforce combinations of each term in the summation to be positive semidefinite such that it obeys the second law.

Appendix B. Discrete residuals and tangents

We use the Galerkin weak form, Eq. (31), for the energy equation and the GGLS formulation, Eq. (32), for the species equations. The GGLS is employed because of its numerical stability property [90]. Using an implicit Euler algorithm with a time step of $\Delta t=t^{n+1}-t^n$, we write $\dot{\theta}=(\theta^{n+1}-\theta^n)/\Delta t$ and $\dot{Y}=(Y^{n+1}-Y^n)/\Delta t$ which yield the residual equations for solving Eqs. (23) and (25) as

$$\begin{aligned}\mathcal{R}_\theta&=\left(u;\rho c\frac{\theta^{n+1}-\theta^n}{\Delta t}\right)+(\nabla u;\lambda\nabla\theta)+(u;\rho D\nabla c\cdot\nabla\theta)\\&\quad+(u;\tilde{j})_{\Gamma^{\mathrm{N}}}+(u;\Delta H_kr_k),\\\mathcal{R}_{Y_{\mathrm{Ni}}}&=\left(v;\rho\frac{Y^{n+1}_{\mathrm{Ni}}-Y^n_{\mathrm{Ni}}}{\Delta t}\right)+(\nabla v;\rho D\nabla Y_{\mathrm{Ni}})+(v;M_{\mathrm{Ni}}r_k),\\\mathcal{R}_{Y_{\mathrm{Al}}}&=\left(v;\rho\frac{Y^{n+1}_{\mathrm{Al}}-Y^n_{\mathrm{Al}}}{\Delta t}\right)+(\nabla v;\rho D\nabla Y_{\mathrm{Al}})+(v;M_{\mathrm{Al}}r_k).\end{aligned} \tag{60}$$

now, we solve the following linear system at each iteration n by the Newton's method

$$\begin{bmatrix}\frac{\partial\mathcal{R}_\theta}{\partial\theta}&\frac{\partial\mathcal{R}_\theta}{\partial Y_{\mathrm{Ni}}}&\frac{\partial\mathcal{R}_\theta}{\partial Y_{\mathrm{Al}}}\\\frac{\partial\mathcal{R}_{Y_{\mathrm{Ni}}}}{\partial\theta}&\frac{\partial\mathcal{R}_{Y_{\mathrm{Ni}}}}{\partial Y_{\mathrm{Ni}}}&\frac{\partial\mathcal{R}_{Y_{\mathrm{Ni}}}}{\partial Y_{\mathrm{Al}}}\\\frac{\partial\mathcal{R}_{Y_{\mathrm{Al}}}}{\partial\theta}&\frac{\partial\mathcal{R}_{Y_{\mathrm{Al}}}}{\partial Y_{\mathrm{Ni}}}&\frac{\partial\mathcal{R}_{Y_{\mathrm{Al}}}}{\partial Y_{\mathrm{Al}}}\end{bmatrix}\begin{bmatrix}\Delta\theta\\\Delta Y_{\mathrm{Ni}}\\\Delta Y_{\mathrm{Al}}\end{bmatrix}=-\begin{bmatrix}\mathcal{R}_\theta\\\mathcal{R}_{Y_{\mathrm{Ni}}}\\\mathcal{R}_{Y_{\mathrm{Al}}}\end{bmatrix}, \tag{61}$$

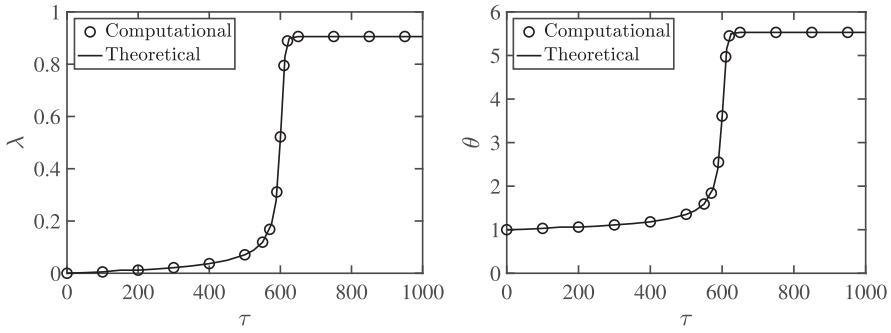

(a) Mass fraction. (b) Temperature.

Fig. 20. Verification of the code for the coupled chemo-thermal solver. (a) shows very good agreement between the theoretical and computational mass fractions and (b) shows excellent agreement between the theoretical and computational temperatures.

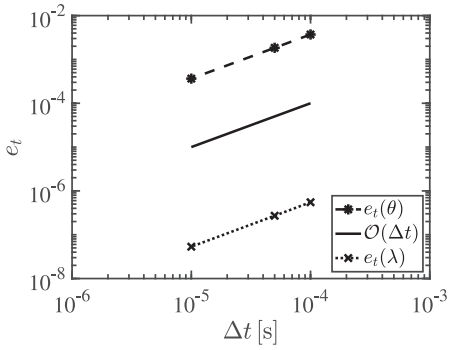

Fig. 21. Time convergence study for the chemo-thermal model. The convergence rates with time refinement for the temperature and mass fractions are 1st order.

where the linearized terms on the left hand side of the system (61) are the Gâteaux derivative of the residuals.

Appendix C. Verification study

Herein, we perform code verification and solution verification [91,92] for the implemented chemo-thermal model.

C.1. Code verification

For the code verification, we adopt the system of equations (1.335–1.337) from Powers [56]. Considering dimensionless parameters $\Theta = 10$, $\eta = 0$, $q = 5$, and $\gamma = 2/5$, the system of equations reduces to the following nonlinear ordinary differential equation

$$\frac{\mathrm{d}\lambda}{\mathrm{d}\tau} = \exp\left[\frac{-10}{1+5\lambda}\right]\left((1-\lambda) - \lambda \exp\left[\frac{-12.5}{1+5\lambda}\right]\right), \ \lambda(0) = 0. \tag{62}$$

Mass fraction λ is solved using Eq. (62) and temperature θ is simply evaluated from Eq. (1.336) in Reference [56]. We compare the theoretical solution to the computational solution of the solver. Figure. 20 shows excellent agreement between the theoretical and computational results. Figure 21 depicts the temporal convergence study. The errors for the temperature and mass fraction with respect to time step are converging at the expected and nearly optimal rates. The errors are computed as

$$e_t(\varphi) = \|\varphi - \varphi^*\|, \tag{63a}$$

where $\|\cdot\|$ is the L_2 norm. Here, φ^* is the theoretical solution while φ is the computational solution. All errors are evaluated at time $t = 600$ s.

C.2. Solution verification

Due to the absence of an analytical solution for the nonlinear problem discussed in Section 4, a self-verification study is performed for the solution verification. We compute the chemo-thermal responses of a premixed system shown in Fig. 3. The spatial and temporal convergence studies are shown in Fig. 22. The errors for the temperature and NiAl mass fraction with respect to the mesh and time refinement are converging at the expected and nearly optimal rates. All errors are calculated at time $t = 3.5$ ms.

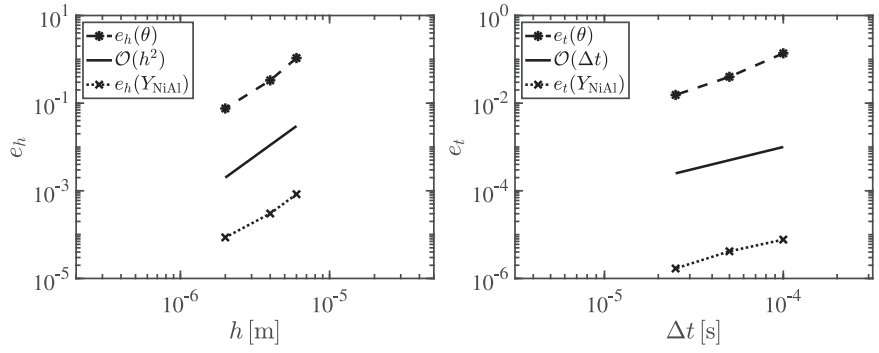

(a) Spatial convergence ($\Delta t = 10^{-4}$). (b) Temporal convergence ($h = 10^{-5}$).

Fig. 22. Spatial and temporal convergence for the premixed Ni–Al reactive sample. All errors are calculated at time $t = 3.5$ ms.

The space and time errors are evaluated as

$$e_h(\varphi) = \|\varphi_h - \varphi_{h_{\text{ref}}}\|, \tag{64a}$$

$$e_t(\varphi) = \|\varphi_t - \varphi_{t_{\text{ref}}}\|, \tag{64b}$$

where $\|\cdot\|$ is the L_2 norm, φ is the relevant field and subscript ref denotes spatial or temporal reference solution. A mesh composed of 100,000 finite elements is used as the spatial reference and a time step of $\Delta t = 1 \times 10^{-5}$ s is used as the temporal reference in Eq. (64).

Supplementary material

Supplementary material associated with this article can be found, in the online version, at doi:10.1016/j.combustflame.2019.05.038.

References

[1] G. Liu, J. Li, K. Chen, Combustion synthesis of refractory and hard materials: a review, Int. J. Refract. Metals Hard Mater. 39 (2013) 90–102.
[2] C.E. Shuck, K.V. Manukyan, S. Rouvimov, A.S. Rogachev, A.S. Mukasyan, Solid-flame: experimental validation, Combust. Flame 163 (2016) 487–493.
[3] K. Morsi, Review: reaction synthesis processing of Ni–Al intermetallic materials, Mater. Sci. Eng.: A 299 (2001) 1–15.
[4] C. Yeh, W. Sung, Combustion synthesis of Ni_3Al intermetallic compound in self-propagating mode, J. Alloys Compd. 384 (2004) 181–191.
[5] X. Su, F. Fu, Y. Yan, G. Zheng, T. Liang, Q. Zhang, X. Cheng, D. Yang, H. Chi, X. Tang, et al., Self-propagating high-temperature synthesis for compound thermoelectrics and new criterion for combustion processing, Nat. Commun. 5 (2014) 1–7.
[6] C. Cannas, A. Musinu, D. Peddis, G. Piccaluga, Synthesis and characterization of $CoFe_2O_4$ nanoparticles dispersed in a silica matrix by a sol–gel autocombustion method, Chem. Mater. 18 (2006) 3835–3842.
[7] M.G. Kim, M.G. Kanatzidis, A. Facchetti, T.J. Marks, Low-temperature fabrication of high-performance metal oxide thin-film electronics via combustion processing, Nat. Mater. 10 (2011) 382–388.
[8] R. Ianos, Highly sinterable cobalt ferrite particles prepared by a modified solution combustion synthesis, Mater. Lett. 135 (2014) 24–26.
[9] M.T. Beason, J.M. Pauls, I.E. Gunduz, S. Rouvimov, K.V. Manukyan, K. Matouš, S.F. Son, A.S. Mukasyan, Shock-induced reaction synthesis of cubic boron nitride, Appl. Phys. Lett. 112 (2018) 171903.
[10] M. S-Shojai, M.T. Khorasani, E. D-Khoshdargi, A. Jamshidi, Synthesis methods for nanosized hydroxyapatite with diverse structures, Acta Biomater. 9 (2013) 7591–7621.
[11] K. Lin, C. Wu, J. Chang, Advances in synthesis of calcium phosphate crystals with controlled size and shape, Acta Biomater. 10 (2014) 4071–4102.
[12] A.G. Merzhanov, The chemistry of self-propagating high-temperature synthesis, J. Mater. Chem. 14 (2004) 1779–1786.
[13] I.E. Gunduz, K. Fadenberger, M. Kokonou, C. Rebholz, C.C. Doumanidis, T. Ando, Modeling of the self-propagating reactions of nickel and aluminum multilayered foils, J. Appl. Phys. 105 (2009) 1–9.
[14] I. Sraj, P. Specht, N. Thadhani, T. Weihs, O. Knio, Numerical simulation of shock initiation of Ni/Al multilayered composites, J. Appl. Phys. 115 (2014) 1–10.
[15] F.T. Li, J. Ran, M. Jaroniec, S.Z. Qiao, Solution combustion synthesis of metal oxide nanomaterials for energy storage and conversion, Nanoscale 7 (2015) 17590–17610.
[16] A.S. Mukasyan, K.V. Manukyan, Combustion/micropyretic synthesis of atomically thin two-dimensional materials for energy applications, Curr. Opin. Chem. Eng. 7 (2015) 16–22.
[17] V. Uskoković, D.P. Uskoković, Nanosized hydroxyapatite and other calcium phosphates: chemistry of formation and application as drug and gene delivery agents, J. Biomed. Mater. Res. Part B: Appl. Biomater. 96 (2011) 152–191.
[18] M.P. Ginebra, C. Canal, M. Espanol, D. Pastorino, E.B. Montufar, Calcium phosphate cements as drug delivery materials, Adv. Drug Deliv. Rev. 64 (2012) 1090–1110.
[19] A. Merzhanov, I. Borovinskaya, Self-spreading high-temperature synthesis of refractory inorganic compounds, Dokl. Akad. Nauk SSSR Seriya Khimiya 204 (1972) 366–369.
[20] A. Varma, A.S. Rogachev, A.S. Mukasyan, S. Hwang, Complex behavior of self-propagating reaction waves in heterogeneous media, Proc. Natl. Acad. Sci. 95 (1998) 11053–11058.
[21] L. Alawieh, T.P. Weihs, O.M. Knio, A generalized reduced model of uniform and self-propagating reactions in reactive nanolaminates, Combust. Flame 160 (2013) 1857–1869.
[22] M. Salloum, O. Knio, Simulation of reactive nanolaminates using reduced models: I. Basic formulation, Combust. Flame 157 (2010) 288–295.
[23] L. Thiers, A.S. Mukasyan, A. Varma, Thermal explosion in Ni-Al system: influence of reaction medium microstructure, Combust. Flame 131 (2002) 198–209.
[24] A. Merzhanov, B. Khaikin, Theory of combustion waves in homogeneous media, Prog. Energy Combust. Sci. 14 (1988) 1–98.
[25] A. Mann, A. Gavens, M. Reiss, D. Van Heerden, G. Bao, T. Weihs, Modeling and characterizing the propagation velocity of exothermic reactions in multilayer foils, J. Appl. Phys. 82 (1997) 1178–1188.
[26] J. Pauls, C. Shuck, A. Rogachev, A. Mukasyan, Micro-heterogeneous regimes for gasless combustion of composite materials, Combust. Sci. Technol. 190 (2018) 893–908.
[27] R. Nikbakht, H. Assadi, Phase-field modelling of self-propagating high-temperature synthesis of NiAl, Acta Mater. 60 (2012) 4041–4053.
[28] A.G. Merzhanov, The theory of stable homogeneous combustion of condensed substances, Combust. Flame 13 (1969) 143–156.
[29] B.V. Novozhilov, Propagation rate of the front of an exothermic reaction in condensed phase, Dokl. Akad. Nauk SSSR 141 (1961) 151–153.
[30] E.I. Maksimov, K.G. Shkadinskii, Steady-state combustion stability of gasless compositions, Combust. Explos. Shock Waves 7 (1971) 392–395.
[31] K.G. Shkadinskii, B.I. Khaikin, A.G. Merzhanov, Propagation of a pulsating exothermic reaction front in the condensed phase, Combust. Explos. Shock Waves 7 (1971) 15–22.
[32] V.A. Vol'pert, A.I. Vol'pert, A.G. Merzhanov, Application of the theory of bifurcations to the investigation of nonstationary combustion regimes, Combust. Explos. Shock Waves 4 (1983) 435–438.
[33] B.I. Khaikin, S.I. Khudyaev, Nonuniqueness of combustion temperature and rate when competing reactions take place, Dokl. Phys. Chem. Acad. Sci. USSR 145 (1979) 225–228.
[34] A. Hardt, P. Phung, Propagation of gasless reactions in solids – I. Analytical study of exothermic intermetallic reaction rates, Combust. Flame 21 (1973) 77–89.
[35] A. Aldushin, B. Khaikin, Combustion of mixtures forming condensed reaction products, Combust. Explos. Shock Waves 10 (1974) 273–280.
[36] R.C. Armstrong, M.L. Koszykowski, Combustion theory for sandwiches of alloyable materials, in: Z.A. Munir, J.B. Holt (Eds.), Combustion and plasma synthesis of high-temperature materials, VCH publisher, New York, 1990, pp. 88–99.
[37] I.E. Gunduz, K. Fadenberger, M. Kokonou, C. Rebholz, C.C. Doumanidis, Investigations on the self propagating reactions of nickel and aluminum multilayered foils, Appl. Phys. Lett. 93 (2008) 1–3.
[38] S. Jayaraman, O. Knio, A. Mann, T. Weihs, Numerical predictions of oscillatory combustion in reactive multilayers, J. Appl. Phys. 86 (1999) 800–809.
[39] A. Hadjiafxenti, I. Gunduz, C. Tsotsos, T. Kyratsi, S. Aouadi, C.C. Doumanidis, C. Rebholz, The influence of structure on thermal behavior of reactive Al–Ni powder mixtures formed by ball milling, J. Alloys Compd. 505 (2010) 467–471.
[40] C. Shuck, A. Mukasyan, Reactive Ni/Al nanocomposites: structural characteristics and activation energy, J. Phys. Chem. A 121 (2017) 1175–1181.
[41] X. Qiu, R. Liu, S. Guo, J.H. Graeter, L. Kecskes, J. Wang, Combustion synthesis reactions in cold-rolled Ni/Al and Ti/Al multilayers, Metal. Mater. Trans. A 40 (2009) 1541–1546.
[42] A. Stover, N. Krywopusk, G. Fritz, S. Barron, J. Gibbins, T. Weihs, An analysis of the microstructure and properties of cold-rolled Ni:Al laminate foils, J. Mater. Sci. 48 (2013) 5917–5929.
[43] R.V. Reeves, A.S. Mukasyan, S.F. Son, Transition from impact-induced thermal runaway to prompt mechanochemical explosion in nanoscaled Ni/Al reactive systems, Propell. Explos. Pyrotech. 38 (2013) 611–621.
[44] I. Gunduz, A. Kyriakou, N. Vlachos, T. Kyratsi, C. Doumanidis, S. Son, C. Rebholz, Spark ignitable Ni–Al ball-milled powders for bonding applications, Surf. Coat. Technol. 260 (2014) 396–400.
[45] C. Shuck, M. Frazee, A. Gillman, M. Beason, I. Gunduz, K. Matouš, R. Winarski, A. Mukasyan, X-ray nanotomography and focused ion beam sectioning for quantitative three-dimensional analysis of nanocomposites, J. Synchrotron Radiat. 23 (2016a) 990–996.
[46] C. Shuck, J.M. Pauls, A. Mukasyan, Ni/Al energetic nanocomposites and the solid flame phenomenon, J. Phys. Chem. C 120 (2016b) 27066–27078.
[47] K. Matouš, M. Geers, V. Kouznetsova, A. Gillman, A review of predictive nonlinear theories for multiscale modeling of heterogeneous materials, J. Comput. Phys. 330 (2017) 192–220.
[48] M. Mosby, K. Matouš, Computational homogenization at extreme scales, Extrem. Mech. Lett. 6 (2016) 68–74.
[49] K. Srinivasan, K. Matouš, P. Geubelle, T. Jackson, Thermomechanical modeling of regressing heterogeneous solid propellants, J. Comput. Phys. 228 (2009) 7883–7901.
[50] D. Yushu, S. Lee, K. Matouš, Sharp volumetric billboard based characterization and modeling of complex 3D Ni/Al high energy ball milled composites, Mech. Mater. 108 (2017) 93–106.
[51] R.C. Smith, Uncertainty quantification: theory, implementation, and applications, SIAM, Philadelphia, 2013.
[52] M.C. Kennedy, A. O'Hagan, Predicting the output from a complex computer code when fast approximations are available, Biometrika 87 (2000) 1–13.
[53] C. Park, R.T. Haftka, N.H. Kim, Remarks on multi-fidelity surrogates, Struct. Multidiscip. Optim. 55 (2017) 1029–1050.
[54] J. Bebernes, D. Eberly, Mathematical problems from combustion theory, Springer-Verlag, New York, 1989.
[55] E.B. Tadmor, R.E. Miller, R.S. Elliott, Continuum mechanics and thermodynamics: from fundamental concepts to governing equations, Cambridge University Press, Cambridge, 2012.

[56] J.M. Powers, Combustion thermodynamics and dynamics, Cambridge University Press, Cambridge, 2016.
[57] R. Bowen, Toward a thermodynamics and mechanics of mixtures, Arch. Ration. Mech. Anal. 24 (1967) 370–403.
[58] R. Atkin, R. Craine, Continuum theories of mixtures: basic theory and historical development, Q. J. Mech. Appl. Math. 29 (1976) 209–244.
[59] F.A. Williams, Combustion theory: the fundamental theory of chemically reacting flow systems, The Benjamin/Cummings, San Francisco, 1985.
[60] S.I. Sandler, Chemical and engineering thermodynamics, John Wiley & Sons, Hoboken, 1989.
[61] G. Hancock, B. McDonnel, Diffusion in the intermetallic compound NiAl, Phys. Status Solidi (A) 4 (1971) 143–150.
[62] G. Erdelyi, D. Beke, F. Kedves, I. Gödény, Determination of diffusion coefficients of Zn, Co and Ni in aluminium by a resistometric method, Philos. Mag. B 38 (1978) 445–462.
[63] S.R. De Groot, P. Mazur, Non-equilibrium thermodynamics, Dover, New York, 1984.
[64] J. Trenkle, L. Koerner, M. Tate, N. Walker, S. Gruner, T. Weihs, T. Hufnagel, Time-resolved x-ray microdiffraction studies of phase transformations during rapidly propagating reactions in Al/Ni and Zr/Ni multilayer foils, J. Appl. Phys. 107 (2010) 113511.
[65] A. Rogachev, S. Vadchenko, F. Baras, O. Politano, S. Rouvimov, A. Mukasyan, Structure evolution and reaction mechanism in the Ni/Al reactive multilayer nanofoils, Acta Mater. 66 (2014) 86–96.
[66] D.R. Lide, CRC handbook of chemistry and physics, national institute of standards & technology, CRC Press, Boca Raton, 2005.
[67] M. Binnewies, E. Milke, Thermochemical data of elements and compounds, Wiley-VCH, Weinheim, 1999.
[68] C. Ho, R. Powell, P. Liley, Thermal conductivity of the elements: a comprehensive review, J. Phys. Chem. Ref. Data (Suppl.) 3 (1974) 1–796.
[69] M. Bauccio, ASM metals reference book, ASM International, Materials Park, 1993.
[70] Y. Terada, K. Ohkubo, T. Mohri, T. Suzuki, Thermal conductivity of intermetallic compounds with metallic bonding, Mater. Trans. 43 (2002) 3167–3176.
[71] D. Shi, B. Wen, R. Melnik, S. Yao, T. Li, First-principles studies of Al–Ni intermetallic compounds, J. Solid State Chem. 182 (2009) 2664–2669.
[72] Y. Wang, Z.K. Liu, L.Q. Chen, Thermodynamic properties of Al, Ni, NiAl, and Ni_3Al from first-principles calculations, Acta Mater. 52 (2004) 2665–2671.
[73] R.A. Adams, J.J. Fournier, Sobolev spaces, 140, Academic Press, Cambridge, 2003.
[74] T.J. Hughes, The finite element method: linear static and dynamic finite element analysis, Dover, New York, 2012.
[75] L.P. Franca, E.G.D. Do Carmo, The Galerkin gradient least-squares method, Comput. Methods Appl. Mech. Eng. 74 (1989) 41–54.
[76] O. Le Maître, O.M. Knio, Spectral methods for uncertainty quantification with applications to computational fluid dynamics, Springer, New York, 2010.
[77] K.V. Manukyan, B.A. Mason, L.J. Groven, Y.C. Lin, M. Cherukara, S.F. Son, A. Strachan, A.S. Mukasyan, Tailored reactivity of Ni + Al nanocomposites: Microstructural correlations, J. Phys. Chem. C 116 (2012) 21027–21038.
[78] K. Hirano, R. Agarwala, M. Cohen, Diffusion of iron, nickel and cobalt in aluminum, Acta Metal. 10 (1962) 857–863.
[79] S. Gennari, U. Tamburini, F. Maglia, G. Spinolo, Z. Munir, A new approach to the modeling of SHS reactions: combustion synthesis of transition metal aluminides, Acta Mater. 54 (2006) 2343–2351.
[80] C. Milanese, Characterization of the steps taking place upon the self-propagating high-temperature synthesis of transition metal silicides, University of Pavia, Italy, 2001 Ph.D. dissertation.
[81] E. Hunt, M. Pantoya, Ignition dynamics and activation energies of metallic thermites: from nano-to micron-scale particulate composites, J. Appl. Phys. 98 (2005) 034909.
[82] B. Adams, L. Bauman, W. Bohnhoff, K. Dalbey, M. Ebeida, J. Eddy, M. Eldred, P. Hough, K. Hu, J. Jakeman, J. Stephens, L. Swiler, D. Vigil, T. Wildey, Dakota: a multilevel parallel object-oriented framework for design optimization, parameter estimation, uncertainty quantification, and sensitivity analysis, Technical Report, National Technology and Engineering Solutions of Sandia, LLC, 2014. Sandia Technical Report SAND2014-4633
[83] Y.M. Marzouk, H.N. Najm, L.A. Rahn, Stochastic spectral methods for efficient Bayesian solution of inverse problems, J. Comput. Phys. 224 (2007) 560–586.
[84] H. Haario, M. Laine, A. Mira, E. Saksman, DRAM: efficient adaptive MCMC, Stat. Comput. 16 (2006) 339–354.
[85] A.S. Shteinberg, Y.C. Lin, S.F. Son, A.S. Mukasyan, Kinetics of high temperature reaction in Ni-Al system: influence of mechanical activation, J. Phys. Chem. A 114 (2010) 6111–6116.
[86] A. Rogachev, S. Vadchenko, A. Mukasyan, Self-sustained waves of exothermic dissolution in reactive multilayer nano-foils, Appl. Phys. Lett. 101 (2012) 063119.
[87] R. Armstrong, Models for gasless combustion in layered materials and random media, Combust. Sci. Technol. 71 (1990) 155–174.
[88] C.E. Rasmussen, Gaussian processes in machine learning: advanced lectures on machine learning, Springer, New York (2004).
[89] P.D. Arendt, D.W. Apley, W. Chen, Quantification of model uncertainty: calibration, model discrepancy, and identifiability, J. Mech. Des. 134 (2012) 100908.
[90] K. Nakshatrala, H. Nagarajan, M. Shabouei, A numerical methodology for enforcing maximum principles and the non-negative constraint for transient diffusion equations, Commun. Comput. Phys. 19 (2016) 53–93.
[91] P.J. Roache, Verification and validation in computational science and engineering, Hermosa, Albuquerque, 1998.
[92] M. Shabouei, K. Nakshatrala, Mechanics-based solution verification for porous media models, Commun. Comput. Phys. 20 (2016) 1127–1162.